Development of a retrofit layer with an embedded array of piezoelectric sensors for transient pressure measurement in maritime applications

Riccioli, Filippo; Huijer, A.J.; Grasso, Nicola; Rizzo, Cesare M.; Pahlavan, Lotfollah

DOI
10.1016/j.marstruc.2023.103395

Publication date
2023

Document Version
Final published version

Published in
Marine Structures

Citation (APA)
Riccioli, F., Huijer, A. J., Grasso, N., Rizzo, C. M., & Pahlavan, L. (2023). Development of a retrofit layer with an embedded array of piezoelectric sensors for transient pressure measurement in maritime applications. *Marine Structures*, *89*, Article 103395. https://doi.org/10.1016/j.marstruc.2023.103395

Marine Structures 89 (2023) 103395

Contents lists available at ScienceDirect

Marine Structures

journal homepage: www.elsevier.com/locate/marstruc

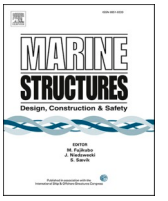

Development of a retrofit layer with an embedded array of piezoelectric sensors for transient pressure measurement in maritime applications

Filippo Riccioli [a,*], Arnaud Huijer [a], Nicola Grasso [b], Cesare M. Rizzo [c], Lotfollah Pahlavan [a]

[a] Department of Maritime and Transport Technology, Delft University of Technology (TU Delft), Delft, the Netherlands
[b] Maritime Research Institute Netherlands (MARIN), Wageningen, the Netherlands
[c] DITEN, University of Genova, Genova, Italy

ARTICLE INFO

Keywords:
Pressure field measurement
Embedded sensor
Spectral element method
Inverse procedure
Piezoelectric sensor

ABSTRACT

Measurement of transient pressure distribution on maritime structures is important for the assessment of the hydrodynamic loads applied. The commonly used pressure sensors are mostly bulky, need to be bolted to the structure, and/or only provide point-wise measurements. In this paper, an elastic matrix layer with a network of embedded piezoelectric sensors is proposed to address these issues. For experimental validation, a 400 × 400 × 5 mm epoxy layer is fabricated embedding 25 piezoelectric sensors on a square grid in accordance with Gauss-Lobatto-Legendre points. A finite element based inverse procedure is developed to reconstruct the pressure field from the electric potentials measured by the piezoelectric transducers. Feasibility of the concept is evaluated by measuring and reconstructing the pressure field generated by a travelling wave in a water tank. Sensitivity of the layer is also investigated through the experiments. The results indicate that the retrofit layer is capable of pressure field reconstruction, and that the presence of disturbances on the sensing surface does not affect the measurements in a notable way, while non-ideal conditions of the mounting can have a significant impact on the accuracy of the measurements. The results highlight the potential of the concept in pressure distribution measurements.

1. Introduction

With the development of sensing systems and the growing interest in non-intrusive loading assessment techniques, interest in embedded sensor networks is growing as well. For maritime structures, embedded solutions enable the monitoring of the assets while protecting the sensors from the environmental conditions. In pressure field assessment and reconstruction, embedded systems represent an innovative and non-intrusive solution compared to the conventional techniques. Measurement of transient pressure distribution on maritime structures is important for assessment of the hydrodynamic loads applied.

Commonly, in maritime applications, pressure measurements are achieved through a set of pressure transducers that are flush-mounted in the structure, e.g. Refs. [1–7]. Conventional pressure sensors often require considerable space to be installed [8], they

* Corresponding author. Building 34, TU Delft, Mekelweg, Delft, 2, the Netherlands.
E-mail addresses: F.Riccioli@tudelft.nl (F. Riccioli), A.J.Huijer@tudelft.nl (A. Huijer), N.Grasso@marin.nl (N. Grasso), Cesare.Rizzo@unige.it (C.M. Rizzo), L.Pahlavan@tudelft.nl (L. Pahlavan).

https://doi.org/10.1016/j.marstruc.2023.103395
Received 10 October 2021; Received in revised form 3 January 2023; Accepted 11 February 2023
Available online 16 February 2023

are bulky, need to be bolted [9], and/or only provide point-wise insights [10].

Typical pressure transducers have a wide application in the experimental investigation of hull pressure pulses induced by marine propeller [2,3], pressure distribution on the bottom of planing vessels [4,5], slamming pressure and/or loads [1,6,7,11–13], and sloshing events [14–21]. As reported by Garme et al. [4], because of the rapid change in hydrodynamic pressure distribution in regular and irregular waves on the bottom of planing vessels, a snapshot of the pressure transducer signals does not give a true picture of the instantaneous distribution unless the transducer matrix is unrealistically dense. Nevertheless, Swidan et al. [6] and Van Wijngaarden et al. [10] highlight the need for accurate pressure field reconstruction, pointing out that the integration of pressures can lead to inaccurate force predictions, unless complete pressure mapping is available. Accomplishing this experimentally on 3D complex hull models is deemed very challenging [6].

Other limitations of commonly used pressure transducers have been reported in literature, such as temperature dependency [22–25] and limited spatial resolution [10,20,26,27]. Furthermore, the use of pressure transducers for a thorough pressure field investigation on a maritime structure is often intrusive [28,29] and additionally, they are expensive to be used in large numbers [28]. Finally, in support of field measurement, extrapolation and interpolation numerical techniques are typically necessary for obtaining a complete description of the pressure field [30]. In other words, to obtain a complete picture of the pressure distribution, either a very large number of transducers or a method to further process the signals is required [8–10,30–34].

Various developments for pressure field reconstruction have been reported in literature, such as pressure mapping systems (PMS) to increase spatial resolution of pressure measurements [26,27], fish lateral-line-inspired pressure sensor arrays for distributed flow reconstruction [35–39], smart pressure transducers using artificial neural network (ANN) to compensate the effect of temperature [22–24], fiber bragg gratings for hull surface pressure measurements [25,40,41], tactile sensors for reconstruction of pressure distribution [29,42], and pressure reconstruction derived from particle image velocimetry (PIV) measurements [43–45].

In this work, we propose an alternative method based on the use of thin piezoelectric sensors embedded in an elastic matrix layer. Piezoelectric materials, at a low electric field intensity [46], provide a linear coupling between the mechanical field to the electrical field and vice versa [47]. Typically, the sensor voltage due to a certain imposed strain field to the structure or the induced strain field of the structure as a function of an imposed electric field are of interest. In these cases, either one-way coupling [48–50] or two-way coupling [46,51] is deployed. Depending on the external conditions, the one-way coupling may be evaluated analytically or numerically, whereas the two-way approach usually involves coupled-field finite element analysis. Often, analytical and numerical approaches are applied to define the sensor behaviour either for a piezoelectric bimorph [52] or an embedded solution [53]. Different authors have highlighted instability issues of the finite element model when considering the electro-mechanical coupling effect, and some studies propose algebraic condensation schemes and dimension-reduction methods as well [54–56]. Smart composite materials have been proposed with embedded piezoelectric transducers [32,50,57–59]. For the same-size piezoelectric sensor, embedded sensors can offer a greater electromechanical coupling than surface-mounted sensors because the sensor is directly influenced by the strain transfer between the host structure and the piezoelectric transducer [50]. Embedded sensors in fiber-reinforced composites [53,59,60] and 3D printed sensors in metallic structures [61] are examples of developments that prove the potential of this technique in the field of maritime structures.

The aim of the present research is to develop a retrofit layer with an embedded array of piezoelectric sensors that can accurately evaluate the transient pressure field distribution. The approach adopted for development of the proposed retrofit layer starts from the mathematical framework of the concept. The spectral element method (SEM) [62–66] and the principles of piezoelectricity [67] are briefly discussed next to provide the mathematical basis for a finite element based inverse procedure. With the support of FE simulations, the design of a flexible and implementable solution is subsequently finalised. An elastic matrix layer with a network of 25 piezoelectric sensors embedded is fabricated. Experiments are designed and performed in order to evaluate the feasibility of the proposed layer and assess its accuracy and sensitivity.

The paper has the following structure. The theoretical framework is presented in section 2. The specimen layout and the description of the manufacturing procedure are given in section 3. Design of the experiments and the related setup are described in section 4. Results are presented and discussed in section 5, followed by conclusions in section 6.

2. Theoretical framework Equation section 2

A multiphysics model for reconstruction of the pressure field from the voltage response of the network of embedded piezoelectric sensors inside a retrofit elastic layer is implemented.

2.1. Description of the approach

The focus is posed on the sensing application of piezoelectric transducers, referred to the direct piezoelectric effect [67]. For low field values, the piezoelectric effect is understood as the linear interaction between mechanical and electrical quantities [46,47]. As a brief background to the behaviour of piezoelectric materials, it is worth to note the two following properties.

- Law of Faraday: a vector quantity $\mathcal{B}$, referred as magnetic flux density, that changes in time t induces electric voltage in a conductive loop

$$\nabla \times \boldsymbol{E} = -\frac{\partial \mathcal{B}}{\partial t} \tag{2.1}$$

where $\boldsymbol{E}$ is the electric field intensity, and $\mathcal{B}$ is the magnetic flux density.

- Law of Gauss: electric charges are the source of the electric field.

$$\nabla \cdot \boldsymbol{D} = q_e \tag{2.2}$$

where $\boldsymbol{D}$ is the electric flux density, and q_e is the volume charge density.

In the static case, the relations above become:

$$\nabla \times \boldsymbol{E} = 0 \tag{2.3}$$

$$\nabla \cdot \boldsymbol{D} = q_e \tag{2.4}$$

Since the electric field vector is irrotational, it can be written in terms of gradient of the so-called electric scalar potential V_e:

$$\boldsymbol{E} = -\nabla V_e \tag{2.5}$$

Considering small deformations in the continuum, the mechanical field is described by linear relations. Navier's equation explains the dynamic behaviour of a solid deformable body of an infinitely small size. The governing equation is:

$$\mathbf{B}^T\boldsymbol{\sigma} + \mathbf{f}_v = \rho_0 \frac{\partial^2 \mathbf{u}}{\partial t^2} \tag{2.6}$$

where ρ_0 stands for the material density and $\mathbf{u} = \{u_x, u_y, u_z\}^T$ denotes the displacement vector. $\mathbf{B}^T$ is the differential operator (transposed) applied on the stress vector $\boldsymbol{\sigma}$ (in Voigt notation), and $\mathbf{f}_v$ represents the prescribed volume forces.

Using the same notation, the relation between the mechanical strain $\boldsymbol{\varepsilon}$ and the displacement $\mathbf{u}$ of an arbitrary point within the deformed solid body is as follows:

$$\boldsymbol{\varepsilon} = \mathbf{B}\mathbf{u} \tag{2.7}$$

where $\mathbf{B}$ is the differential operator and $\boldsymbol{\varepsilon}$ is the strain vector containing the six independent components (Voigt notation) of the strain tensor.

The constitutive equations of piezoelectricity relate stress $\boldsymbol{\sigma}$ and electric displacement $\boldsymbol{D}$ to strains $\boldsymbol{\varepsilon}$ and electric field intensity $\boldsymbol{E}$, respectively. For small variations in the above parameters, these equations are considered linear [53], and in Voigt notation are expressed as:

$$\boldsymbol{\sigma} = \boldsymbol{c}^{\mathrm{E}}\boldsymbol{\varepsilon} - \boldsymbol{e}^T\boldsymbol{E} \tag{2.8}$$

$$\boldsymbol{D} = \boldsymbol{e}\boldsymbol{\varepsilon} + \boldsymbol{g}^{\varepsilon}\boldsymbol{E} \tag{2.9}$$

where $\boldsymbol{c}^{\mathrm{E}}$ is the elasticity matrix under constant electric field, $\boldsymbol{e}$ the piezoelectric constant matrix, and $\boldsymbol{g}^{\varepsilon}$ the dielectric constant matrix under constant strain.

2.2. Spectral element method (SEM) for forward simulation

Using high-order one-dimensional Lagrange polynomial and its tensor product, the displacement field in finite elements is approximated as follows:

$$\begin{Bmatrix} u^{\mathrm{e}}(\xi,\eta,\zeta) \\ v^{\mathrm{e}}(\xi,\eta,\zeta) \\ w^{\mathrm{e}}(\xi,\eta,\zeta) \end{Bmatrix} = \mathbf{N}^{\mathrm{e}}\widehat{\mathbf{u}}^{\mathrm{e}} = \sum_{k=0}^{n}\sum_{j=0}^{n}\sum_{i=0}^{n} N_i^{\mathrm{e}}(\xi)N_j^{\mathrm{e}}(\eta)N_k^{\mathrm{e}}(\zeta)\mathbf{I_3} \begin{Bmatrix} \widehat{u}^{\mathrm{e}}(\xi_i,\eta_j,\zeta_k) \\ \widehat{v}^{\mathrm{e}}(\xi_i,\eta_j,\zeta_k) \\ \widehat{w}^{\mathrm{e}}(\xi_i,\eta_j,\zeta_k) \end{Bmatrix} \tag{2.10}$$

where N_i^{e} is the one-dimensional shape function (nth-order Lagrange interpolation function at $n+1$ Gauss-Lobatto-Legendre points) of the isoparametric element [68], and $\widehat{u}^{\mathrm{e}}$ represents the nodal degrees of freedom.

Considering small deformation, the linear strains are approximated as:

$$\boldsymbol{\varepsilon}(\xi,\eta,\zeta) = \mathbf{B}_{\mathrm{u}}^{\mathrm{e}}\widehat{\mathbf{u}}^{\mathrm{e}} \tag{2.11}$$

where $\mathbf{B}_{\mathrm{u}}^{\mathrm{e}}$ is the strain-nodal displacement matrix:

$$\mathbf{B}_{\mathrm{u}}^{\mathrm{e}} = \mathbf{L}\mathbf{N}^{\mathrm{e}}(\xi,\eta,\zeta) \tag{2.12}$$

$$\mathbf{L}=\begin{bmatrix} \frac{\partial}{\partial x} & 0 & 0 & \frac{\partial}{\partial y} & 0 & \frac{\partial}{\partial z} \\ 0 & \frac{\partial}{\partial y} & 0 & \frac{\partial}{\partial x} & \frac{\partial}{\partial z} & 0 \\ 0 & 0 & \frac{\partial}{\partial z} & 0 & \frac{\partial}{\partial y} & \frac{\partial}{\partial x} \end{bmatrix}^T \begin{Bmatrix} \frac{\partial}{\partial x} \\ \frac{\partial}{\partial y} \\ \frac{\partial}{\partial z} \end{Bmatrix} = \mathbf{J}^{-1} \begin{Bmatrix} \frac{\partial}{\partial \xi} \\ \frac{\partial}{\partial \eta} \\ \frac{\partial}{\partial \zeta} \end{Bmatrix} \tag{2.13}$$

where $\mathbf{J}$ is the Jacobi matrix.

Using (2.5) and electric field approximation, the electric field vector can be related to the electric potential field $\widehat{\varphi}$ as follows:

$$\boldsymbol{E} = -\mathbf{B}_{\varphi}\widehat{\varphi} \tag{2.14}$$

where $\mathbf{B}_{\varphi}$ is the electric field potential matrix calculated as:

$$\mathbf{B}_{\varphi} = \begin{Bmatrix} \frac{\partial}{\partial x} & \frac{\partial}{\partial y} & \frac{\partial}{\partial z} \end{Bmatrix}^T \mathbf{N}^{\mathrm{e}}(\xi,\eta,\zeta) \tag{2.15}$$

The governing equations of motion are achieved by means of the material law of piezoelectricity, (2.8) and (2.9). Inserting the material law into Navier's equation (2.6) as well as into the Law of Gauss (2.4), the coupled partial differential equations, (2.18) and (2.19), for displacement $\mathbf{u}$ and electric potential V_e respectively are obtained:

$$\mathbf{B}^T\left(\boldsymbol{c}^{\mathrm{E}}\boldsymbol{\varepsilon} - \boldsymbol{e}^T\boldsymbol{E}\right) + \mathbf{f}_{\mathrm{v}} = \rho_0\ddot{\mathbf{u}} \tag{2.16}$$

$$\nabla\cdot\left(\boldsymbol{e}\boldsymbol{\varepsilon} + \boldsymbol{g}^{\varepsilon}\boldsymbol{E}\right) = q_e \tag{2.17}$$

$$\rho_0\ddot{\mathbf{u}} - \mathbf{B}^T\left(\boldsymbol{c}^{\mathrm{E}}\mathbf{B}\mathbf{u} + \boldsymbol{e}^T\nabla V_e\right) = \mathbf{f}_{\mathrm{v}} \tag{2.18}$$

$$\nabla\cdot\left(\boldsymbol{e}\mathbf{B}\mathbf{u} - \boldsymbol{g}^{\varepsilon}\nabla V_e\right) = q_e \tag{2.19}$$

where the relations (2.5) and (2.7) have been applied to eqs. (2.16) and (2).17).

By applying a test function for the displacement and for the electric potential, the weak form of the above equations is derived, leading in few steps to the algebraic system of equations in matrix form:

$$\mathbf{M}^{\mathrm{e}}\ddot{\widehat{\mathbf{u}}}^{\mathrm{e}} + \mathbf{K}^{\mathrm{e}}_{uu}\widehat{\mathbf{u}}^{\mathrm{e}} - \mathbf{K}^{\mathrm{e}}_{u\varphi}\widehat{\varphi}^{\mathrm{e}} = \mathbf{f}^{\mathrm{e}} \tag{2.20}$$

$$\mathbf{K}^{\mathrm{e}}_{\varphi u}\widehat{\mathbf{u}}^{\mathrm{e}} - \mathbf{K}^{\mathrm{e}}_{\varphi\varphi}\widehat{\varphi}^{\mathrm{e}} = \mathbf{q}^{\mathrm{e}} \tag{2.21}$$

where $\mathbf{M}^{\mathrm{e}}$ denotes the element mass matrix, $\mathbf{K}^{\mathrm{e}}_{uu}$ the element stiffness matrix, $\mathbf{K}^{\mathrm{e}}_{u\varphi}$ and $\mathbf{K}^{\mathrm{e}}_{\varphi u}$ the piezoelectric coupling matrices, $\mathbf{K}^{\mathrm{e}}_{\varphi\varphi}$ the dielectric permittivity matrix, $\widehat{\varphi}^{\mathrm{e}}$ the elementary potential vector, $\mathbf{f}^{\mathrm{e}}$ the nodal external force vector, and $\mathbf{q}^{\mathrm{e}}$ the nodal externally applied charge vector.

The matrices and vectors in (2.20), (2.21) are defined as:

$$\mathbf{M}^{\mathrm{e}} = \int_{V^e}\mathbf{N}_u^T\rho_0\mathbf{N}_u dV^{\mathrm{e}} \tag{2.22}$$

$$\mathbf{K}^{\mathrm{e}}_{uu} = \int_{V^e}\mathbf{B}_u^T\boldsymbol{c}^{\mathrm{E}}\mathbf{B}_u dV^{\mathrm{e}} \tag{2.23}$$

$$\mathbf{K}^{\mathrm{e}}_{u\varphi} = -\int_{V^e}\mathbf{B}_u^T\boldsymbol{e}^T\mathbf{B}_{\varphi} dV^{\mathrm{e}} \tag{2.24}$$

$$\mathbf{K}^{\mathrm{e}}_{\varphi u} = \mathbf{K}^{\mathrm{e}}_{u\varphi} \tag{2.25}$$

$$\mathbf{K}^{\mathrm{e}}_{\varphi\varphi} = \int_{V^e}\mathbf{B}_{\varphi}^T\boldsymbol{g}\mathbf{B}_{\varphi} dV^{\mathrm{e}} \tag{2.26}$$

$$\mathbf{f}^{\mathrm{e}} = \int_{V^e}\mathbf{N}_u^T\mathbf{P}_b dV^{\mathrm{e}} + \int_{\Gamma_S}\mathbf{N}_u^T\mathbf{P}_S d\Gamma_S + \mathbf{P}^{\mathrm{e}} \tag{2.27}$$

$$\mathbf{q}^{e} = \int_{\Gamma_\varphi} \mathbf{N}_\varphi^T \mathbf{q}_0 d\Gamma_\varphi \tag{2.28}$$

where $\mathbf{N}_u$ and $\mathbf{N}_\varphi$ are the matrices of the shape functions, $\mathbf{P}_b$ and $\mathbf{P}_S$ are the respective body and surface force vectors, V^e and Γ_S are the finite element volume and surface respectively, and $\mathbf{q}_0$ is the vector of the externally applied charge over the boundary Γ_φ [65].

After the global matrices are assembled, the vector of unknown displacements and potentials can be directly solved. However, for the piezoelectric materials, typical element values of $\mathbf{K}_{uu}^{e}$ are of the order 10^8, while typical element values of $\mathbf{K}_{\varphi\varphi}^{e}$ are the order 10^{-11} [55]. This relevant difference in magnitude would make the global matrices too ill-conditioned if the two governing equations of motion are taken as a whole. To overcome this problem, the general method of static condensation by matrix algebra is adopted. In the present study, the unknown potentials are sacrificed in favour of the unknown displacements.

Considering the sensing application of piezoelectric transducers, the governing equations of motion (2.20) and (2.21) are condensed as:

$$\mathbf{M}^{e}\ddot{\widehat{\mathbf{u}}}^{e} + \left(\mathbf{K}_{uu}^{e} + \mathbf{K}^{S}\right)\widehat{\mathbf{u}}^{e} = \mathbf{f}^{e} \tag{2.29}$$

where $\mathbf{K}^S$ denotes the induced mechanical stiffness matrix due to the electromechanical coupling of the piezoelectric materials which depends on electric boundary condition (open circuit, closed circuit, actuator).

The evaluation of the induced mechanical stiffness matrix $\mathbf{K}^S$ is complicated because the elementary dielectric permittivity matrix $\mathbf{K}_{\varphi\varphi}^{e}$ in (2.21) is not positive definite. To make static condensation possible, electric boundary conditions must be applied so that the reduced elementary dielectric permittivity matrix will be positive definite and the unknown potentials can be solved in terms of elementary displacements using (2.21).

Since the piezoelectric materials can be used as sensors either in closed circuit or in open circuit and/or as actuators, three different electric boundary conditions can be considered. As suggested by Wang [55], $\mathbf{K}^S$ can be written as:

$$\mathbf{K}^{S} = \mathbf{K}_c + \mathbf{K}_o + \mathbf{K}_a \tag{2.30}$$

where $\mathbf{K}_c$, $\mathbf{K}_o$ and $\mathbf{K}_a$ are the corresponding induced stiffness of the piezoelectric transducers in closed circuit, in open circuit, and as actuator respectively.

Considering the piezoelectric open circuit sensor, the electric potential at the bottom surface of the sensor is assumed zero (grounded). The electric potential vector consequently becomes $\widehat{\varphi}^{e} = \{\,0 \quad \widehat{\varphi}_o\,\}^T$, where $\widehat{\varphi}_o$ is the induced open-circuit sensor potential vector. Then, the charge equation (2.21) for the open circuit case can be written as:

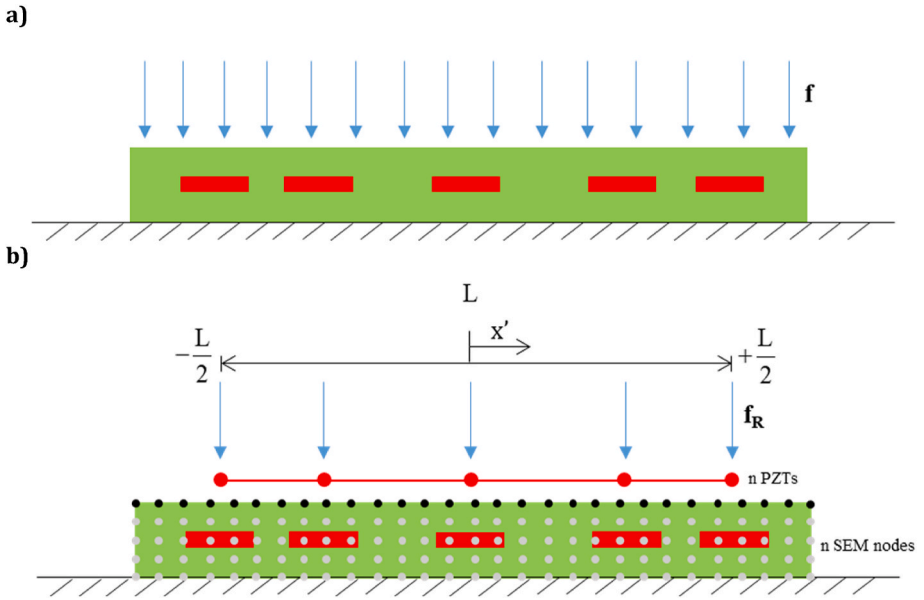

Fig. 1. (**a**) Bidimensional scheme of an elastic layer (green area) with a number of piezoelectric sensors (red squares) embedded, subject to a force distribution **f** (blue arrows). (**b**) Reduced discretisation scheme (red circular nodes) coinciding with the number (n PZTs) and locations of embedded piezoelectric sensors for pressure field on the bidimensional elastic layer surface. Note that the bidimensional elastic layer is discretized with n SEM nodes.

$$\mathbf{K}^{e}_{\varphi u}\widehat{\mathbf{u}}^{e}-\mathbf{K}^{e}_{\varphi\varphi}\begin{Bmatrix}0\\ \widehat{\varphi}_{o}\end{Bmatrix}=\begin{Bmatrix}q_{0}\\ 0\end{Bmatrix} \tag{2.31}$$

where $\widehat{\varphi}_{o}$ can be obtained by solving the above equation:

$$\widehat{\varphi}_{o}=\left(\mathbf{K}^{o}_{\varphi\varphi}\right)^{-1}\mathbf{K}^{o}_{\varphi u}\widehat{\mathbf{u}}^{e} \tag{2.32}$$

in which $\mathbf{K}^{o}_{\varphi\varphi}$ and $\mathbf{K}^{o}_{\varphi u}$ are the corresponding sub-matrices of $\mathbf{K}^{e}_{\varphi\varphi}$ and $\mathbf{K}^{e}_{\varphi u}$, respectively. Finally, the induced stiffness of the piezoelectric sensor in open circuit assumption can be formulated as

$$\mathbf{K}^{S}=\mathbf{K}_{o}=-\left(\mathbf{K}^{o}_{\varphi u}\right)^{T}\left(\mathbf{K}^{o}_{\varphi\varphi}\right)^{-1}\left(\mathbf{K}^{o}_{\varphi u}\right) \tag{2.33}$$

Based on eqs. (2.32) and (2).33), the inverse procedure to pressure field reconstruction is derived.

2.3. Inverse procedure to pressure field reconstruction

An inverse procedure is proposed to reconstruct the pressure field applied on the layer from the electric potentials measured by the piezoelectric sensors. To explain the procedure and the mathematical formulation, it is convenient to start from the bidimensional case, considering an elastic layer with a number of arbitrary-positioned piezoelectric sensors inside (Fig. 1a).

Considering the sensing equation (2.32), the relation between the nodal displacements and the electric potentials can be expressed as follows:

$$\mathbf{\Omega u}=\mathbf{v}_{\mathbf{measured}} \tag{2.34}$$

where $\mathbf{u}$ is the nodal displacements vector due to external forces, $\mathbf{v}_{\mathbf{measured}}$ is the measured voltages vector, and $\mathbf{\Omega}$ is the combination of different operators that will be explained below.

In the quasi-static case, the nodal displacements can be written in terms of external forces using the inverse of the SEM global stiffness matrix, then equation (2.34) becomes

$$\mathbf{\Omega K}^{-1}\mathbf{f}=\mathbf{v}_{\mathbf{measured}} \tag{2.35}$$

where $\mathbf{K}^{-1}$ is the inverse of global stiffness matrix and $\mathbf{f}$ is the external force vector (Fig. 1a).

In order to perform an inverse operation, a reduced discretisation scheme for the pressure field at the surface is introduced (Fig. 1b).

The reduced discretisation scheme allows obtaining a correspondence between the number of known electric potentials and the number of unknown external loads: there will be as many grid points as the number of sensors (Fig. 1b).

The pressure distribution can be described on the reduced basis using the following equation:

$$f(x')=\mathbf{N}\mathbf{f}_{\mathbf{R}} \tag{2.36}$$

where $\mathbf{N}$ is evaluated using $n_{PZT}-1$ order Lagrange polynomials, and $\mathbf{f}_{\mathbf{R}}$ is the reduced force vector (Fig. 1b). The above equation can be expanded as follows:

$$\mathbf{f}_{\mathbf{surface}}=\begin{Bmatrix}f\left(x'=-\frac{L}{2}\right)\\ \vdots\\ f\left(x'=\frac{L}{2}\right)\end{Bmatrix}=\begin{bmatrix}\mathbf{N}\left(x'=-\frac{L}{2}\right)\\ \vdots\\ \mathbf{N}\left(x'=\frac{L}{2}\right)\end{bmatrix}\mathbf{f}_{\mathbf{R}} \tag{2.37}$$

$$\mathbf{f}_{\mathbf{surface}}=\begin{bmatrix}N_{1}\left(x'=-\frac{L}{2}\right) & \cdots & N_{n_{PZT}}\left(x'=-\frac{L}{2}\right)\\ \vdots & \ddots & \vdots\\ N_{1}\left(x'=\frac{L}{2}\right) & \cdots & N_{n_{PZT}}\left(x'=\frac{L}{2}\right)\end{bmatrix}\mathbf{f}_{\mathbf{R}} \tag{2.38}$$

$$\mathbf{f}_{\mathbf{surface}}=\mathbf{P}_{\mathbf{surface}}\mathbf{f}_{\mathbf{R}} \tag{2.39}$$

where L is the length of the reduced discretisation scheme (Fig. 1b).

Then, the projection matrix $\mathbf{P}$ contains the evaluation of the reduced space on the coordinate x' of each surface node of the global model, $\mathbf{P}_{\mathbf{surface}}$, and the Boolean matrix, $\mathbf{I}_{\mathbf{P}}$:

$$\mathbf{P}=\mathbf{I}_{\mathbf{P}}\mathbf{P}_{\mathbf{surface}} \tag{2.40}$$

Including the reduced force vector, equation (2.35) becomes:

$$\mathbf{\Omega K^{-1} P f_R = v_{measured}} \tag{2.41}$$

A Boolean operator $\mathbf{\Gamma}$ is defined to sub-select the piezoelectric element nodal displacements from the global nodal displacements vector:

$$\mathbf{\Omega \Gamma K^{-1} P f_R = v_{measured}} \tag{2.42}$$

where:

$$\mathbf{K^{-1} P f_R = u_{global}} \tag{2.43}$$

where $\mathbf{u_{global}}$ is the global nodal displacements vector.

The resulting vector from this selection contains the nodal displacements of each piezoelectric element $\mathbf{u}^{e}_{PZT_n}$, with $n = n_{PZT}$ components:

$$\mathbf{\Gamma K^{-1} P f_R} = \begin{Bmatrix} \mathbf{u}^{e}_{PZT_1} \\ \mathbf{u}^{e}_{PZT_2} \\ \vdots \\ \mathbf{u}^{e}_{PZT_n} \end{Bmatrix} \tag{2.44}$$

Following the standard FEM procedure, mechanical boundary conditions are applied to evaluate the displacements from the external force vector. Then, the SEM global stiffness matrix is reduced accordingly as also the shape of the matrices $\mathbf{\Gamma}$ and $\mathbf{P}$ is influenced.

A matrix operator is introduced to obtain the voltage values from the piezoelectric element nodal displacements. From the sensing equation (2.32), the sensing matrix is defined.

$$\mathbf{\Psi} = -\left(\mathbf{K}^{o}_{\varphi\varphi}\right)^{-1}\mathbf{K}^{o}_{\varphi u} \tag{2.45}$$

The sensing matrix is also rearranged accordingly, as follows:

$$\mathbf{\Phi} = \begin{bmatrix} \mathbf{\Psi} & 0 & 0 & 0 & 0 & 0 \\ 0 & \mathbf{\Psi} & 0 & 0 & 0 & 0 \\ 0 & 0 & \mathbf{\Psi} & 0 & 0 & 0 \\ 0 & 0 & 0 & \mathbf{\Psi} & 0 & 0 \\ 0 & 0 & 0 & 0 & \mathbf{\Psi} & 0 \\ 0 & 0 & 0 & 0 & 0 & \mathbf{\Psi} \end{bmatrix} \tag{2.46}$$

Hence, equation (2.42) becomes:

$$\mathbf{\Phi \Gamma K^{-1} P f_R = v_{measured}} \tag{2.47}$$

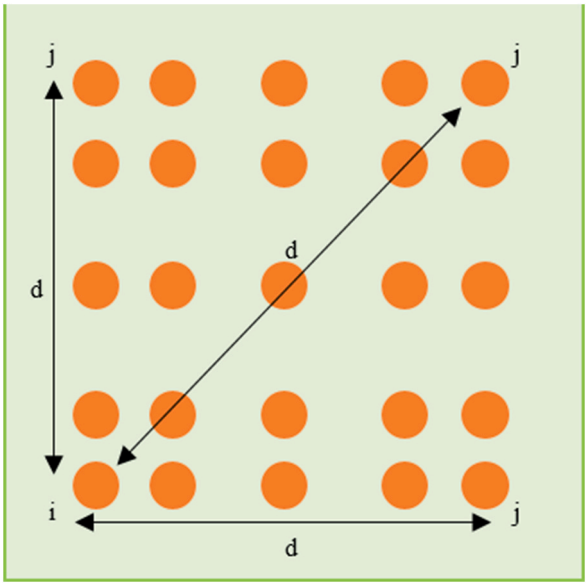

Fig. 2. Planar scheme of the elastic layer with a network of piezoelectric sensors embedded.

The final formulation of the inverse procedure in the bi-dimensional case is presented as:

$$\mathbf{H}\mathbf{f}_{\mathbf{R}} = \mathbf{v}_{\mathbf{measured}} \tag{2.48}$$

where $\mathbf{H}$ is the stiffness matrix.

Solving the system of equations, the reduced force vector is obtained as:

$$\mathbf{f}_{\mathbf{R}} = \mathbf{H}^{-1}\mathbf{v}_{\mathbf{measured}} \tag{2.49}$$

and using the projection matrix, the external force vector is evaluated:

$$\mathbf{f} = \mathbf{P}\mathbf{f}_{\mathbf{R}} \tag{2.50}$$

which describes the force distribution on the SEM 2D grid on the surface.

The solution of the inverse procedure is needily extended to the 3D case considering a planar scheme of the elastic layer with an embedded network of piezoelectric sensors (Fig. 2).

Recalling eq. (2.48) and using the index notation, the inverse problem is written as follows:

$$\sum_{j}^{n_{sensors}} H_{ij}(d) f_{Rj} = v_{measured_i} \tag{2.51}$$

where $v_{measured_i}$ is the voltage measured by the i-th piezoelectric sensor, f_{Rj} is the force applied on the j-th piezoelectric sensor, and $H_{ij}(d)$ is the 'influence coefficient' as function of the distance d between i-th sensors and j-th sensor (Fig. 2).

The matrix operator H_{ij} is named 'influence coefficients' matrix. It expresses how much the force applied on the j-position sensor contributes to the voltage output of the i-position sensor. Solving the above system of equations, the full distribution of force over the network of sensors is obtained using the projection matrix.

Knowing the force distribution, a conversion is necessary to obtain the pressure distribution. The relation between pressure and force is expressed using the scalar λ.

$$\mathbf{p} = \begin{Bmatrix} p_1 \\ p_2 \\ \vdots \\ p_n \end{Bmatrix} = \lambda \begin{Bmatrix} f_1 \\ f_2 \\ \vdots \\ f_n \end{Bmatrix} = \lambda \mathbf{f} \tag{2.52}$$

To retrieve the above coefficient, it can be stated that the integral of the pressure field evaluated over the surface of the elastic layer (A_{patch}) is equal to the total force that is expressed as the sum of all components of the force vector.

$$\int_{A_{patch}} p(x,y)dxdy = F_{tot} = \sum f_i \tag{2.53}$$

Using finite element formulation, the pressure field is written as product of shape functions and nodal values.

$$\int_{A_{patch}} p(x,y)dxdy = \int_{A_{patch}} \mathbf{N}\mathbf{p}dxdy \tag{2.54}$$

Then, substituting the initial assumption into eq. (2.54):

$$\int_{A_{patch}} \mathbf{N}\mathbf{p}dxdy = \lambda \int_{A_{patch}} \mathbf{N}\mathbf{f}dxdy \tag{2.55}$$

which leads to the evaluation of the scalar:

$$\lambda = \frac{\sum f_i}{\int_{A_{patch}} \mathbf{N}\mathbf{f}dxdy} = \frac{\sum f_i}{\left(\int_{A_{patch}} \mathbf{N}dxdy\right)\mathbf{f}} \tag{2.56}$$

Once the conversion scalar is evaluated, it can be applied during the processing of all the experimentally measured data.

2.4. Evaluation of the influence coefficient matrix

To calculate the components of the influence coefficient matrix for the elastic layer, the analytical formulation proposed by Gopalakrishnan et al. [49] is applied for retrieving the voltage generated by piezoelectric sensor of arbitrary shape from the strains components.

Consider the constitutive equation for the piezoelectric domain in eq. (2.9) in sensing mode.

The dimension of the problem is reduced by considering a number of assumptions. Polarization of the piezoelectric material is

assumed along its thickness direction x_3 resulting in two zero components of the electric displacement vector ($D_1 = D_2 = 0$). Plain strain assumption is also considered for the piezoelectric sensor element. Equation (2.9) can be accordingly reduced and then rewritten considering the following strain-charge form of the piezoelectric constitutive equations:

$$D_3 = \varphi(x)\mathbf{b}^T\left[\gamma(x)\boldsymbol{d}^{\sigma}\boldsymbol{c}^{E}\boldsymbol{\varepsilon} + \left(\boldsymbol{g}^{\sigma} - \boldsymbol{d}^{\sigma}\boldsymbol{c}^{E}\boldsymbol{d}^{\sigma^T}\right)\boldsymbol{E}\right], x \in \Theta \tag{2.57}$$

where $\mathbf{b} = [0,0,1]^T$, while, $\boldsymbol{d}^{\sigma}$ and $\boldsymbol{g}^{\sigma}$ respectively denote the matrix of the piezoelectric strain constants and of the permittivity constants evaluated at constant stress. The two introduced functions, $\gamma(x)$ and $\varphi(x)$, depend on the location in the domain Θ and they present the following values:

$$\gamma(x) = \pm 1, x \in \Theta_{PZT} \tag{2.58}$$

depending on the polarization distribution in the domain of the piezoelectric sensor Θ_{PZT}, and:

$$\varphi(x) = \begin{cases} 1, & x \in \Theta_{PZT} \\ 0, & x \in \Theta - \Theta_{PZT} \end{cases} \tag{2.59}$$

which describes the shape of the piezoelectric patch.

For further elaboration on derivation of eq. (2.57)-(2.59), Gopalakrishnan et al. [49] is recommended.

Considering the sensing application, the total charge developed over the piezoelectric area is zero. Then, integration of both sides of eq. (2.57) gives:

$$\mathbf{b}^T\boldsymbol{d}^{\sigma}\boldsymbol{c}^{E}\int_{\Theta}\boldsymbol{\varepsilon}\varphi(x)\gamma(x)dx = \mathbf{b}^T\left(\boldsymbol{d}^{\sigma}\boldsymbol{c}^{E}\boldsymbol{d}^{\sigma^T} - \boldsymbol{g}^{\sigma}\right)\int_{\Theta}\varphi(x)\boldsymbol{E}dx \tag{2.60}$$

where constant piezoelectric properties are considered over the piezoelectric domain. By imposing $E_1 = E_2 = 0$ and the linear distribution of voltage across the thickness of the piezo element, the electric field vector in equation (2.60) can be expressed as:

$$\boldsymbol{E} = \frac{V}{t_P}\mathbf{b} \tag{2.61}$$

Then, substituting in eq. (2.60) and solving for the measured voltage V results in:

$$V = \frac{t_P}{A_P\left[\mathbf{b}^T\left(\boldsymbol{d}^{\sigma}\boldsymbol{c}^{E}\boldsymbol{d}^{\sigma^T} - \boldsymbol{g}^{\sigma}\right)\mathbf{b}\right]}\mathbf{b}^T\boldsymbol{d}^{\sigma}\boldsymbol{c}^{E}\int_{\Theta}\boldsymbol{\varepsilon}\varphi(x)\gamma(x)dx \tag{2.62}$$

where $A_P = \int_{\Theta}\varphi(x)dx$ is the area covered by the piezoelectric element [49]. The components of the influence coefficients matrix in eq. (2.51) can be calculated using eq. (2.62) as discussed in section 5.1.

In summary, to reconstruct the transient pressure distribution from the measured voltages, firstly the reduced force vector is calculated using eq. (2.49). Secondly, the external force vector is evaluated using eq. (2.50). Finally, the pressure distribution results from a scalar conversion, as presented in eq. (2.52).

3. Retrofit sensor layer

3.1. Selection of transducers

Disc-shaped piezoelectric sensors with wrap-around electrodes on the faces of the disc were used. The dimensions of the disc were 10 mm in diameter and 0.2 mm in thickness. In total, 25 piezoelectric sensors were embedded in the host material.

The piezoelectric material used is PIC255, a product of PI Ceramic. This is a “soft” PZT material, providing large piezoelectric charge coefficient, moderate permittivity and high coupling factors [69], with a Curie temperature and a recommended maximum operating temperature of 350 °C and 175 °C [70], both higher than the host material curing temperature.

3.2. Design of sensors layout

A 2D FE model of a representative specimen of resin with one piezoelectric sensor embedded has been developed in order to

Table 1
Electromechanical, mechanical and electrical material properties of PZ27 piezoceramic [72]. Permittivity ε_r^T is relative to the permittivity of vacuum and determined at zero stress T. Subscript 1 relates to both in-plane directions, while subscript 3 refers to the out-of-plane direction.

Name	d_{31}, d_{33}, d_{15} [$\times 10^{-9}$ C/m]	$s_{11}^E, s_{12}^E, s_{13}^E, s_{11}^E, s_{33}^E, s_{44=55}^E, s_{66}^E$ [$\times 10^{-12}$ m^2/N]	$\varepsilon_{11,r}^T, \varepsilon_{33,r}^T$ [$\times 10^3$]
PZ27	−17, 42.5, 50.6	17, −6.6, −8.61, 23.2, 43.5, 47.1	1.8, 1.8

identify the vertical position within the thickness of the layer that provides the highest voltage output from a reference load. The host material has a horizontal extension of 65 mm and a thickness of 5 mm, while the PZT element has a length of 5 mm and a thickness of 0.5 mm, and is horizontally located at the centre of the specimen. Assumed material properties of the host material are: E = 3.5 GPa, ν = 0.33, ρ = 1540 kg/m^3. Material properties of the considered piezoelectric material are given in Table 1.

A compressional point force is applied on the upper surface of the host material right above the centre of the PZT element. The vertical position of the sensor is varied between 1.0 mm and 4.50 mm, being the distance measured from the bottom surface of the host material to the upper surface of the piezoelectric element (Fig. 3a–b). The elements size is 5 × 0.5 mm and 4th order polynomials are used to describe the field variable in the element domain (Fig. 3c). Plane stress assumption is made.

The simulation has been performed with eight different vertical positions of the PZT sensor. This investigation implies that placing the sensors approximately embedded 0.5 mm below the upper surface of the layer provides the highest voltage output in this case (Fig. 3a–c).

The final design of the layer, as given in Fig. 4, shows the 25 piezoelectric sensors placed on a square grid in accordance with Gauss-Lobatto-Legendre points. This design choice allowed implementing a slim numerical routine for evaluation of the transient pressure field distribution by using the SEM element interpolants.

3.3. Fabrication of the layer

For the realization of the layer, a 400 × 400 mm aluminium mould was assembled (Fig. 5). Guidelines for the sensors layout were scribed on the fabricated mould (Fig. 6).

Before manufacture the layer, the piezoelectric sensors were prefabricated (Fig. 7).

To obtain a waterproof link between the network of sensors and the data acquisition system, a combination of bifilar copper wiring and a network of flat ribbon cables has been used (Fig. 8). In this way, each sensor is linked to a copper wire that has been soldered to the ends of the ribbon cable. All these parts end up being embedded in the host material, while the other terms of the ribbon cable have been completed by applying appropriate pins to be connected to the data acquisition system. As a result, five rows of sensors have been obtained. To ease the installation of the embedded hardware, five cut-outs have been realized on one side of the mould corresponding to the positions of the rows of sensors.

In the first stage of the manufacturing process, the setup was prepared by insulating the mould to prevent leakage of resin, installing the prefabricated sensors, and mixing the POLY-POX 500 Epoxy resin with the hardener (Fig. 9).

In a second stage, a 4 mm thick layer of resin was poured and cured for 4 h at room temperature, i.e. 18° to 20 °C. In a third stage, the sensors were placed in the designed positions (Fig. 10) and a 1 mm thick layer of resin was poured. It has been noted that after pouring 1 mm thick layer of resin the piezoelectric sensors slightly moved upwards from their original position and eventually tilted.

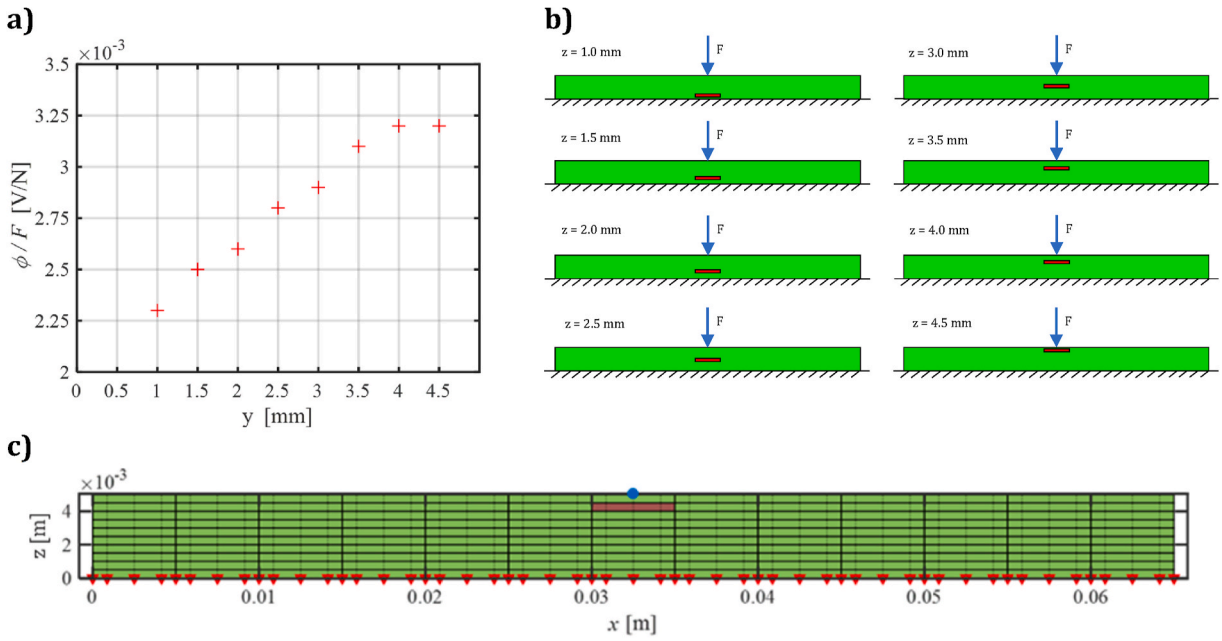

Fig. 3. (**a**) Electric potential output as function of the vertical position of the piezoelectric transducer. (**b**) Schematic illustration of the FE model varying the position of the piezoelectric element (red square) in the thickness direction of the host material (green area) with a compressional point force (blue arrow) applied on the upper surface of the host material. (**c**) Sample of the FE calculation model. The upper surface of the piezoelectric element (red square) is distant 0.5 mm from the upper surface of the host material (green area). Compressional point force (blue node) is applied on the upper surface of the host material. Fixed boundary conditions (red triangles) at the bottom surface of the host material are applied.

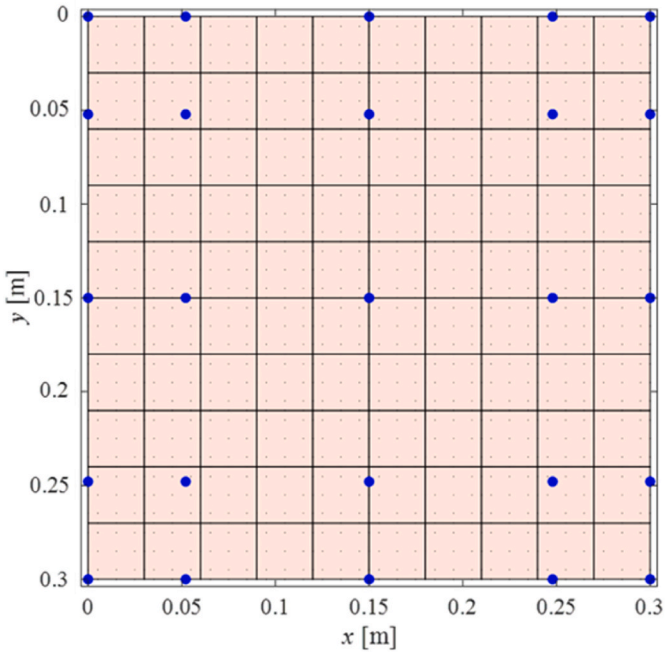

Fig. 4. Retrofit layer layout with 5 × 5 nodes discretisation scheme.

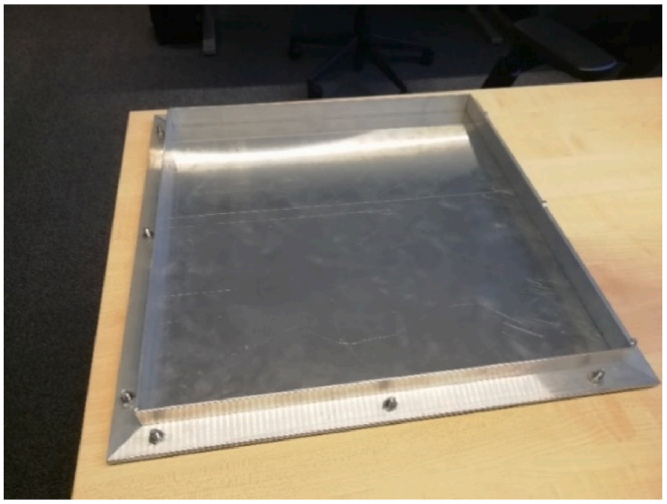

Fig. 5. Aluminium mould.

Once the epoxy resin was cured, the layer was pulled out of the mould for obtaining the final product (Figs. 11–12). All the flat ribbon cables were successfully embedded into the resin resulting in a solid watertight connection between the network of sensors and the data acquisition system (Fig. 12). After the curing process, the vertical position of the piezoelectric sensors was noted to be between 0 and 1 mm from the upper surface of the host material due to the variations in position during the fabrication.

The quality of the installation of the embedded sensors has been further assessed by visual inspection after fabrication. Condition of the sensors has been classified into three groups (Table 2), being correctly positioned (CP), tilted (T), not available (NA).

For quality control, thickness of the layer has been quantified on various locations of it (Fig. 13) providing an indication of the flatness of the retrofit layer. Measurements have been performed using a calibrated SAUTER TN-EE Ultrasonic Thickness Gauge. Table 3 summarizes the thickness measurements for each location shown in Fig. 13. The mean, standard deviation, and maximum variation of the thickness measurements were 5.17 mm, 0.374 mm, and 0.140 mm, respectively.

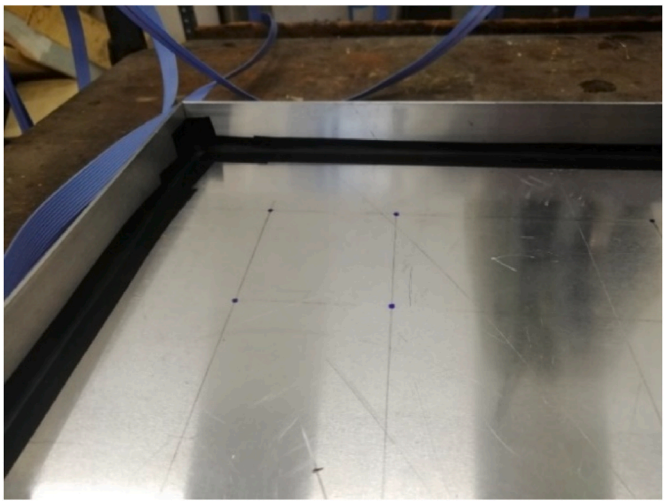

Fig. 6. Scribed guidelines for sensors layout.

Fig. 7. Prefabricated sensors.

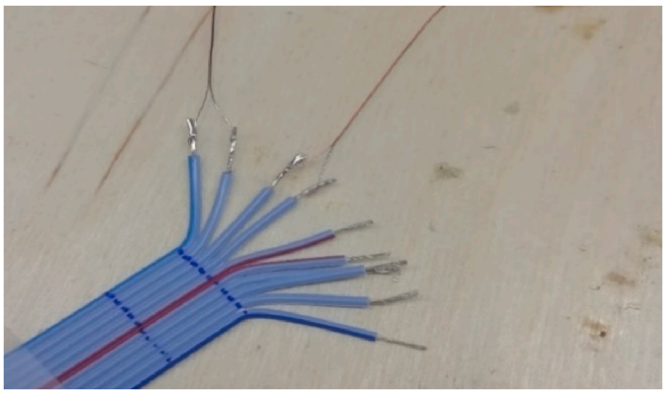

Fig. 8. Bifilar copper wire and flat ribbon cable.

4. Experiments

4.1. Experimental setup

To evaluate the capabilities of the layer, experiments were performed involving measurement and reconstruction of a pressure field

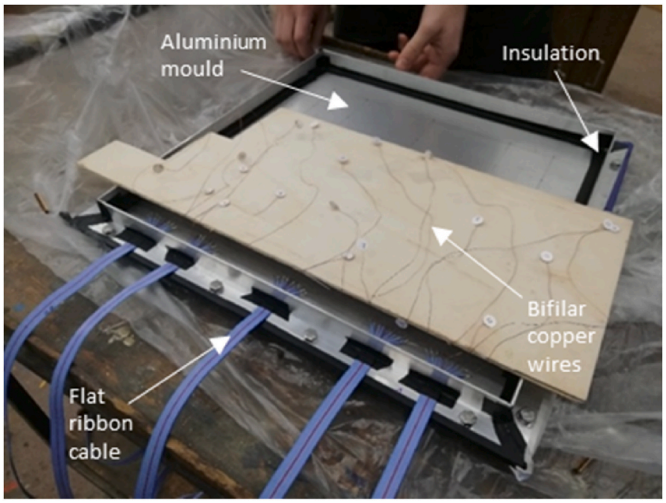

Fig. 9. Installation of network of sensors.

Fig. 10. Placing of the PZT sensors.

generated by a travelling wave in a water tank. The experiments also aimed to provide insights into the sensitivity of the concept and its possible calibration.

The experiments were conducted in an 800 × 500 × 400 mm water tank provided by the Maritime Research Institute Netherlands (MARIN). Fig. 14 shows a schematic overview of the experimental setup.

To replicate a recognizable pressure field, a travelling wave was created using a mechanical pressure pulse generator (Fig. 15). The layer with the embedded network of piezoelectric sensors was placed with the sensing surface facing the bottom of the tank where the pulse generator was located. Also, the position of the layer along the length of the tank (L = 800 mm, Fig. 14) was such that during the experiment, firstly a concentrated pressure could be created on the initial portion of the surface and, secondly, the excitation of the remaining portion of the layer could be done by the travelling wave.

During the experiments, the layer was supported by a base frame in order to maintain the desired boundary conditions (Fig. 16). The layer was clamped at its borders and sustained by a support plate in order to avoid bending behaviour due to the pressure field. Although the support plate had finite stiffness, it is considered to be sufficient to support the layer and minimize the influence of the bending behaviour. The effect of bending on the measured voltages and the reconstructed pressure field is discussed in section 5.3.

The structure was designed to be versatile and easy to assemble. The frame allowed to change the position of the layer, both in terms of immersion depth and in terms of longitudinal position along the length of the tank (Fig. 14). The upper part of the structure was realized using two 1400 mm wood beams supported by the sides of the tank, and four 1000 mm steel threaded rods to adjust the vertical asset of the setup. The submerged part of the frame, with the purpose of reproducing the desired boundary conditions, was assembled using a 400 × 400 mm composite flat plate and four aluminium U profiles (25 × 25 × 2 mm). For each U profile, three holes

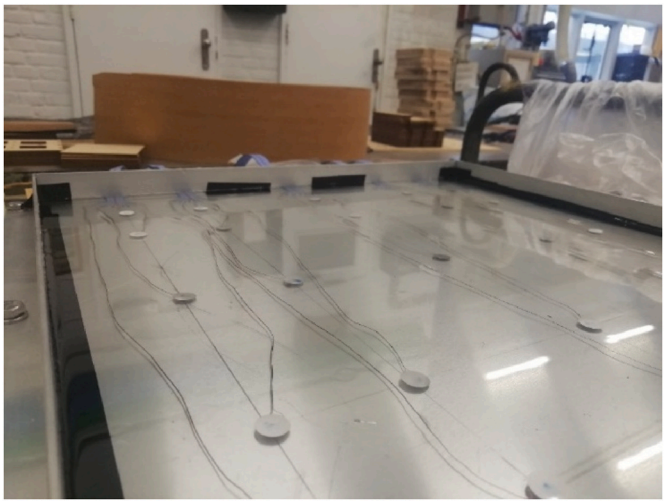

Fig. 11. Fully cured retrofit sensor layer.

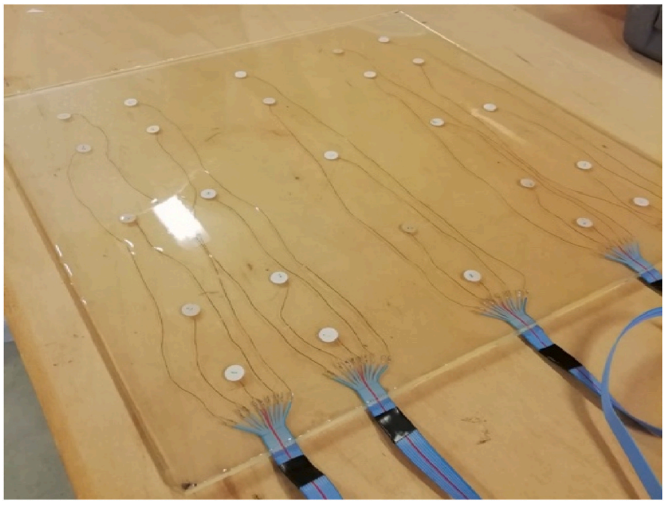

Fig. 12. Retrofit sensor layer.

Table 2
Results of visual inspection of the embedded piezoelectric sensors. Tilt of the sensors refers to less than 30° of inclination with respect to the horizontal plane. Non-working sensors have been classified as not available.

Name	Group	Name	Group	Name	Group	Name	Group	Name	Group
PZT 1	T	PZT 6	NA	PZT 11	T	PZT 16	CP	PZT 21	CP
PZT 2	CP	PZT 7	CP	PZT 12	CP	PZT 17	CP	PZT 22	CP
PZT 3	T	PZT 8	CP	PZT 13	CP	PZT 18	NA	PZT 23	T
PZT 4	CP	PZT 9	T	PZT 14	CP	PZT 19	NA	PZT 24	CP
PZT 5	CP	PZT 10	T	PZT 15	T	PZT 20	CP	PZT 25	CP

were drilled on one side of it so that it could be possible to clamp the layer and the support plate by tightening bolts.

The designed mechanical pressure pulse generator was based on the physical principle of a wave generation by sudden energy release underwater. The mechanical wave generator was created with an acrylic flexible plate and two PVC plates (600 × 190 × 10 mm and 60 × 190 × 10 mm, Fig. 15), all of them assembled using bolts. With the use of a small piece of PVC, the acrylic plate was bolted in correspondence with one end of the PVC base plate, while the other end of the flexible acrylic plate was held in place by screws wedged in the base plate. To generate the wave in each part of the experiment, the free end of the acrylic plate was mechanically unlocked from the constrain, releasing then energy at the bottom of the water volume.

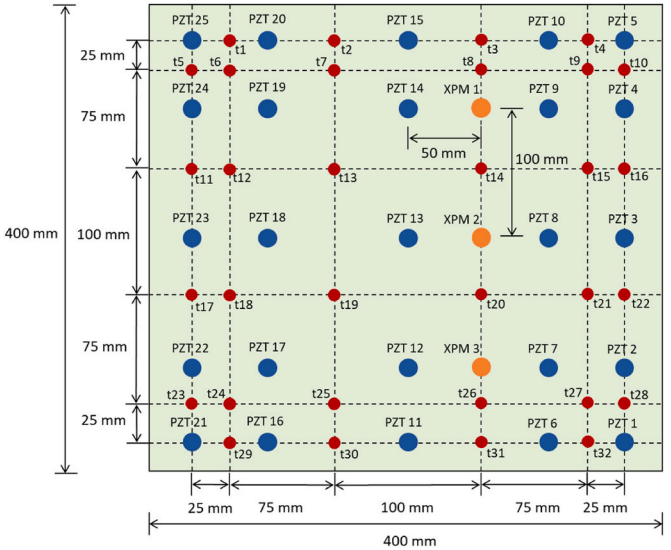

Fig. 13. Schematic illustration of the piezoelectric sensors locations and numbering, and thickness measurements locations on the surface of the layer.

Table 3
Thickness measurements results.

Name	t [mm]	Name	t [mm]	Name	t [mm]	Name	t [mm]
t1	5.05	t9	4.56	t17	5.59	t25	5.58
t2	4.96	t10	4.49	t18	5.53	t26	5.41
t3	4.80	t11	5.43	t19	5.30	t27	5.39
t4	4.39	t12	5.33	t20	5.18	t28	5.23
t5	5.20	t13	5.25	t21	5.05	t29	5.76
t6	5.14	t14	4.95	t22	4.95	t30	5.64
t7	4.99	t15	4.78	t23	5.76	t31	5.45
t8	4.71	t16	4.70	t24	5.69	t32	5.20

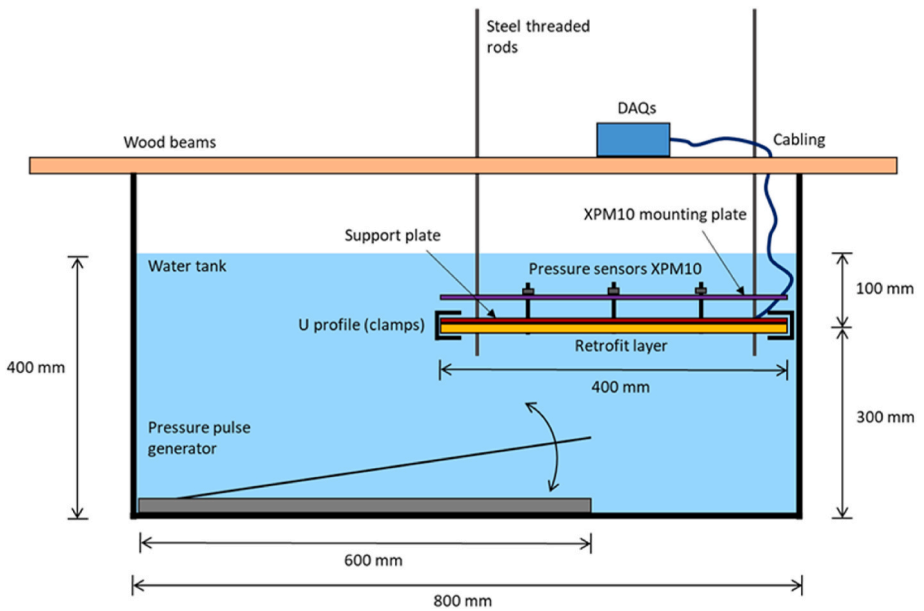

Fig. 14. Schematic overview of the experimental setup.

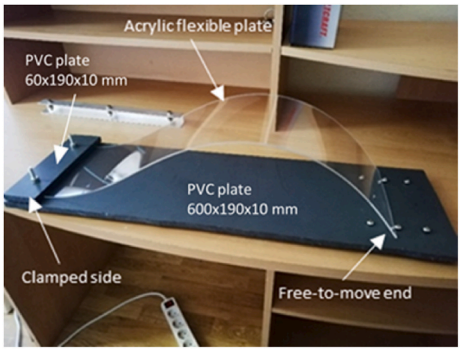

Fig. 15. Mechanical pressure pulse generator.

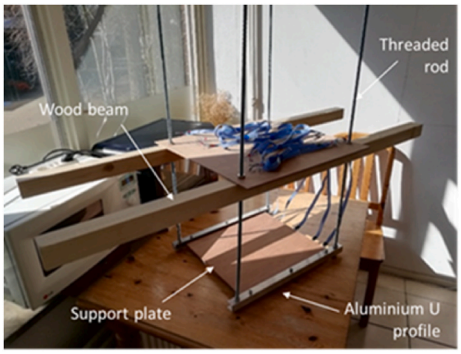

Fig. 16. Assembly of the supporting base frame (only two aluminium U profiles are shown. Four profiles in total have been used during the experiments).

4.2. Data acquisition, management, quality control

The setup described above was complemented by two NI USB-6211 data acquisition systems. One system managed fifteen piezoelectric sensors and the other one handled the remaining ten sensors. Both systems connected to a common ground. Electrical resistance of piezoelectric sensors and data acquisition system were in the range of 10^9-10^{10} and above 10^9 respectively [71]. The sampling frequency was set to 1000 Hz. Given the frequency range of interest between 2.5 and 20 Hz, a band-pass filter was applied on the response signals before using them for the evaluation of the pressure field distribution.

Fig. 17. XPM10 M10 flush pressure sensor.

To validate the performances of the designed layer in terms of pressure signals magnitude and phase, reference measurements have also been performed using miniature dynamic pressure sensors. *XPM10 M10 flush* sensors have been used for this purpose (Fig. 17) connected to a separate data acquisition system provided by MARIN (Fig. 18).

The experiments setup described is section 4.1 has been modified accordingly to allow simultaneous pressure measurements with XPM10 and retrofit layer. Three holes have been drilled into the layer and an additional mounting plate in order to allocate the pressure gauges (Fig. 19). The set of XPM10 has been bolted to the mounting plate and flush mounted with the layer (Fig. 20).

The locations of the three XPM10 with respect to the embedded piezoelectric sensors are depicted in Figs. 13 and 27.

The updated configuration of the experiments setup allowed performing pressure measurements with the two systems in parallel during the experiment described in section 4.1 limiting the uncertainties due to the repeatability of the test.

A sampling frequency equal to 1000 Hz for both the XPM10 and the layer has been used to sample the data during the experiment. The inverse procedure presented in section 2.3 has been applied to reconstruct the pressure field from the voltages measured by the piezoelectric sensors. The three localized pressure signals have been extrapolated from the pressure field reconstruction and compared to the measurements performed by the respective pressure sensors.

A qualitative sensitivity study has been performed simulating the non-perfect conditions of the setup and evaluating the influence of disturbances that can be present in reality.

- Debris on the layer (captured by adding extra interference on the sensing surface)
- Mounting surface imperfections (captured by modification of the back of the layer)

The first condition aims to simulate the behaviour of the layer with presence of hypothetical marine growth. The second case considers the chance of mounting the layer on a non-perfectly flat surface.

The designed setup with no additional disturbance has been considered as the reference case, i.e. *Base case*. The sensing surface of the layer was cleaned and the layer was clamped to the intact support plate. To simulate debris on the layer, fabric sheets (Fig. 21) were interposed before the sensing surface, i.e. *One ply of fabric, Two plies of fabric, Three plies of fabric*. To replicate the behaviour of the layer mounted on a non-ideal wall, the intact support plate was substituted with three bands composite supports (Fig. 22), i.e. Three point support plate. Furthermore, the extreme condition was also tested by removing all the support plates from the setup, i.e. No support plate. This modifications implies that the results will be affected by the bending behaviour of the layer (which was not allowed in the original setup).

5. Results and discussion

5.1. Numerical simulations

Following the modelling procedure, a numerical routine is implemented to process the data obtained from the experiments. First, evaluation of the influence coefficient matrix is performed by means of modelling the 3D layer and using the analytical formulation presented in section 2.4 to retrieve the voltage from the strain components. Secondly, based on the in-plane geometry of the layer, the projection matrix is computed.

Starting from the measured voltages, the procedure adopted to reconstruct the pressure field involves two mathematical operators. The first one transforms the measured voltages into virtual point forces (2.49) while the second one projects the 25 virtual point forces to pressure distribution over the surface of the layer (2.50).

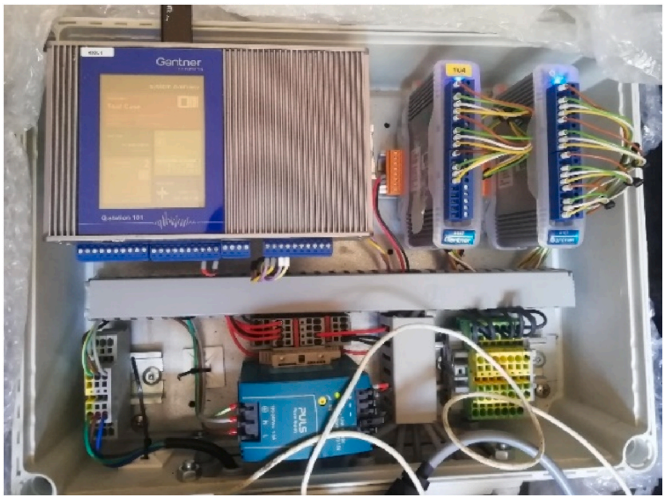

Fig. 18. DAQs of XPM10 pressure sensors.

Fig. 19. Three XPM10 bolted to the mounting plate.

Fig. 20. Sample of flush mounted pressure sensors.

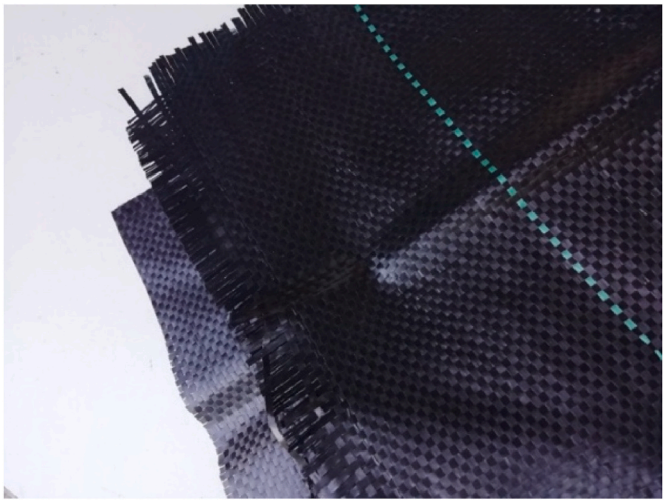

Fig. 21. Sample of fabric sheets.

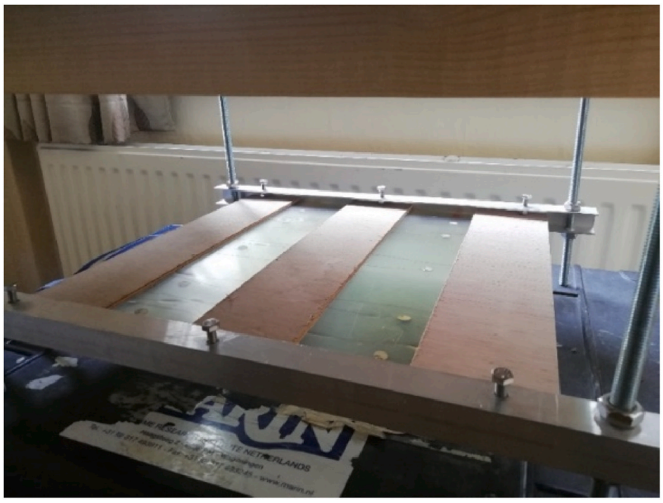

Fig. 22. Three bands composite support plate.

To shape the matrix operator that converts the measured voltages to the external applied forces, it must be defined how much the force applied on the j-position sensor contributes to the voltage output of the i-position sensor. A 3D FE model of the layer has been realized. An external unit force has been applied to the node at x = y = 180 mm. A square element has been used to represent the piezoelectric sensor. The 400 × 400 × 5 mm geometry of the layer was discretized with 100 volumetric 3D elements. In the thickness direction only one element was used. The elements size was 40 × 40 × 5 mm and 4th order polynomials in the x-direction (width) and z-direction (length) were used to describe the field variable in the element domain. A convergence study has been performed to select the order of polynomials in y-direction (thickness). Polynomials up to 6th order were tested in the simulations. The 4th order polynomials have been considered as a good compromise between the accuracy and the CPU memory usage. Assumed material properties were in accordance with the values listed in section 3.2.

In Fig. 23 the top and side view of the elastic matrix layer is shown. The unit nodal force applied is represented by the red mark. The nodes of the element of interest are highlighted with blue circles. This element is representative of a piezoelectric transducer. The resulting displacements and strains of the selected element have been processed by means of the formulation presented in section 2.4.

Varying the in-plane distance between the applied force and the transducer, the following result has been obtained (Fig. 24). The value of the influence coefficient is maximum at zero (force applied above the sensor) and it decreases when moving away from the application point.

Based on the distance between the sensors that compose the network, the matrix operator has been shaped. The dimension of the H matrix operator is [25 × 25], since it relates the point force at the location of one sensor to the voltages measured by all the transducers. From Fig. 25 diagonal shape of the influence coefficients matrix is reported.

The diagonal shape of the influence coefficients matrix suggests that only the point forces acting on the piezoelectric sensor location contribute to the voltage measured by the sensors itself. Limited influence between the point force and the voltages measured by the

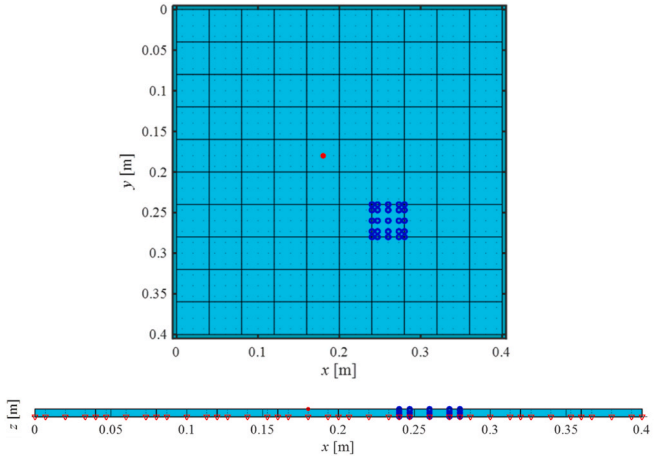

Fig. 23. Top and side view of the elastic matrix layer FE model.

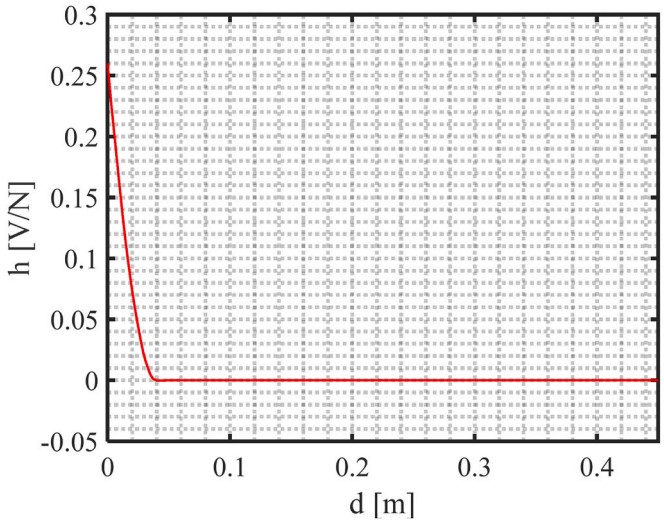

Fig. 24. Influence coefficient vs. distance from the punctual force.

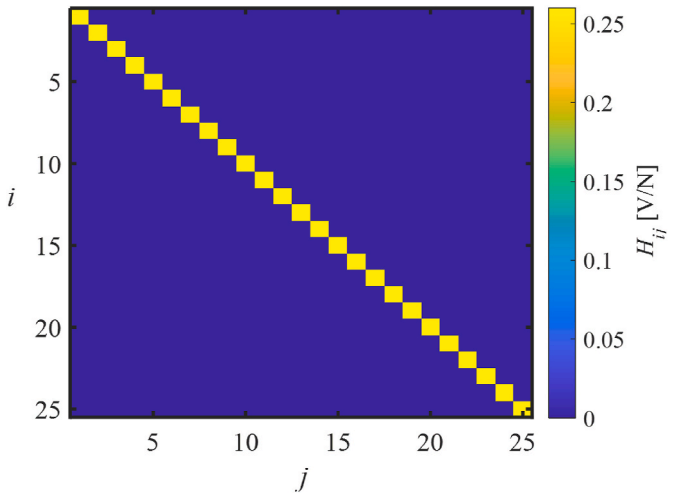

Fig. 25. Influence coefficient matrix.

other transducers has been found. Based on the designed sensors layout and the result presented in Fig. 24, it appears that the influence coefficient drops to zero when reaching d = 0.05 m (minimum distance between two adjacent piezoelectric sensors). The result is considered valid for the specific host material in use. Materials softer than the deployed epoxy resin would allow to higher influence coefficients. It must be noted that eq. (2.51), presented in section 2.3, is proposed for the very general case and still remains valid in the presented case study.

The projection operator has been shaped from the surface geometry of the layer. Two discretisation schemes have been applied. First, a 10 × 10 SEM elements (with 4th order polynomials in x- and y-directions) mesh has been used to model the layer surface. Secondly, a 5 × 5 grid of nodes has been used to discretize the pressure field. As discussed earlier, the location of the surface nodes is the same as the sensors (Fig. 4).

The present model allows obtaining a matrix that can link the two discretisation models (of the surface and the body of the layer). Combining the polynomial shape functions of the two mesh schemes, the mathematical operator has been shaped.

5.2. Pressure field measurement and reconstruction

Two NI USB-6211 data acquisition systems have been used to collect the experimental data. Due to the bias of the two boards, the raw data have been lined up to the horizontal axis subtracting the mean of the entire time series. After this step, a windowing function has been applied in order to prepare the signals for band-pass filtering (2.5–20 Hz).

An example of the 25 voltage signals measured by the embedded network of transducers is reported in Fig. 26b. The presented

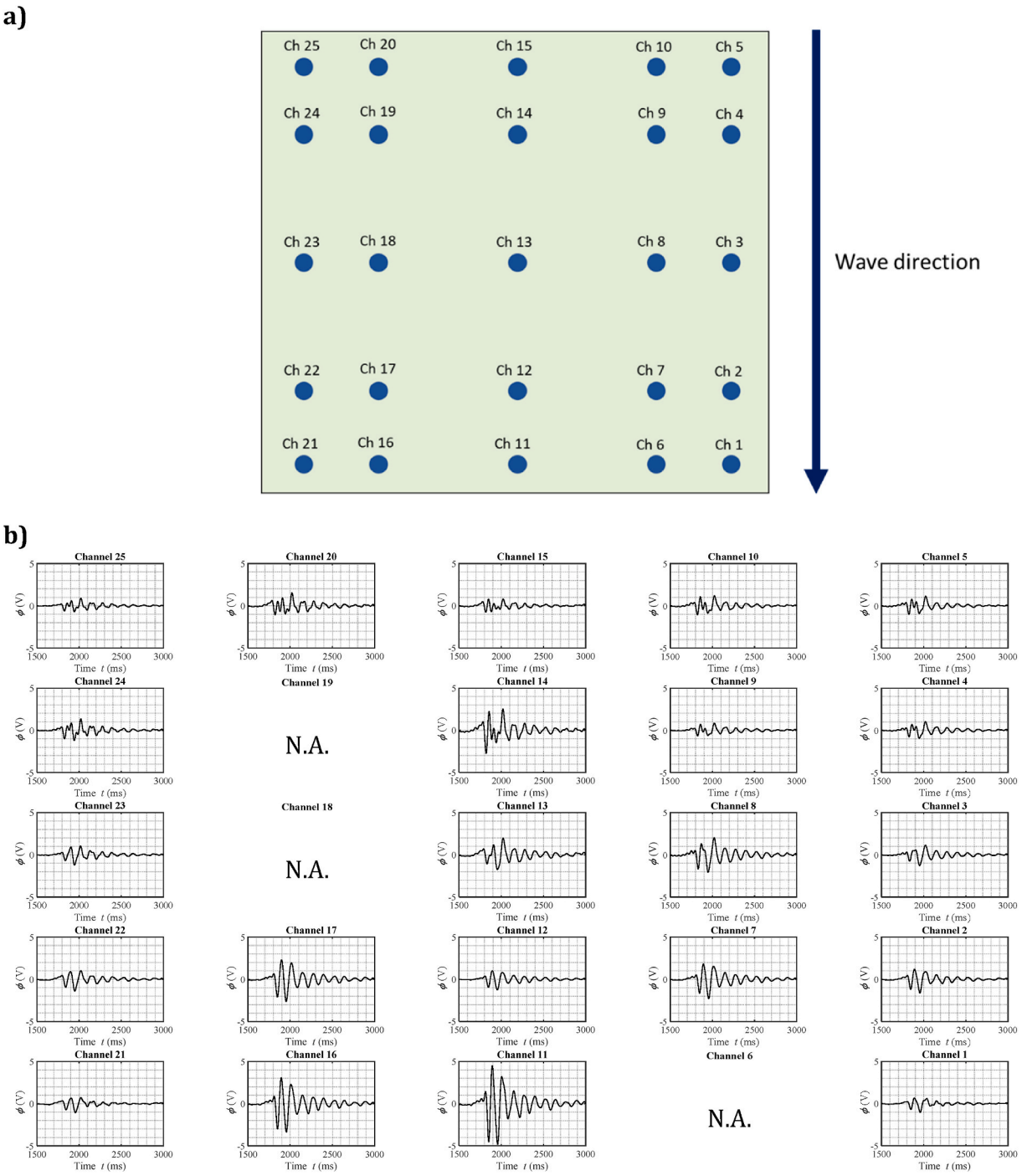

Fig. 26. (**a**) Schematic overview of channels numbering. (**b**) Sample of 25 voltage signals measured by the embedded network of piezoelectric sensors.

signals are the results obtained from the data processing mentioned above. A first negative voltage peak is present in all the time series, typically followed by a second negative peak. The former is representative of the relevant travelling pressure wavefield, while the latter is more likely related to reflection of the pressure wavefield coming perpendicularly to the vertical side of the tank. It is notable that the amplitude of the second peak is dominant in the channels located on the layer side close to the flank of the water tank (two rows at the lower part of the sensors grid, see Fig. 26a), and it decreases when moving towards the top part of the layer, i.e. channels 5-10-15-20-25.

It should be mentioned also that sensors 6, 18, and 19 were malfunctioning due to damage of the PZT electrodes during the

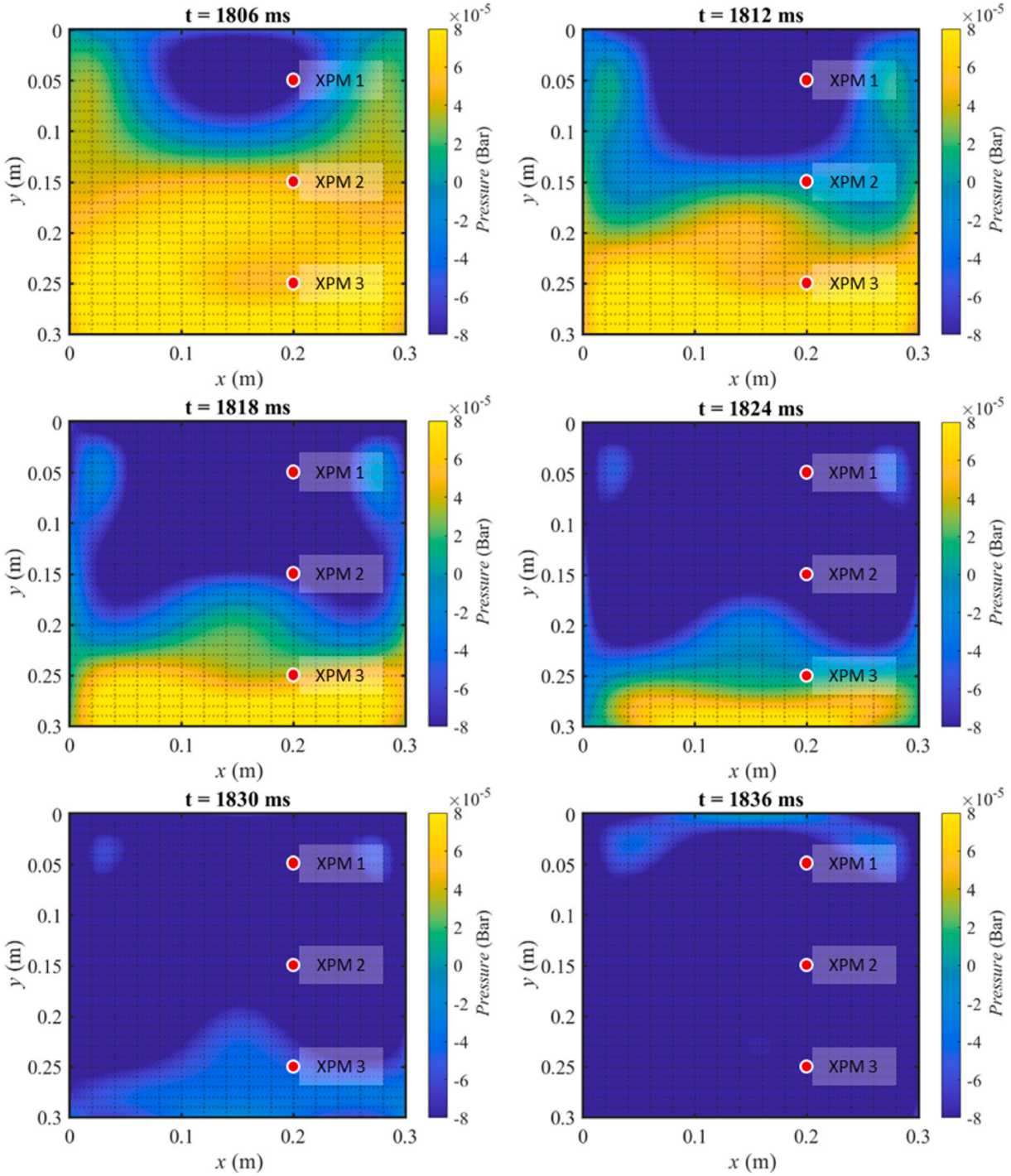

Fig. 27. Sample of pressure wavefield reconstruction. Locations of the three pressure sensors (XPM10 M10 flush) used as reference measurements are indicated by red closed circles ($x_1 = x_2 = x_3 = 0.2$ m, $y_1 = 0.05$ m; $y_2 = 0.15$ m, $y_3 = 0.25$ m).

fabrication of the layer. Based on the observed symmetrical behaviour of the generated pressure wavefield, symmetry (with respect to y-axis) assumption has been applied to the damaged sensor locations, i.e. missing measuring points. Note that the rest of the sensors in the network also confirm the general symmetric behaviour of the induced pressure wave.

Once the voltage signals have been pre-processed, the developed routine can be applied to the data for obtaining the final reconstruction of the pressure field. Firstly, the influence coefficient matrix is used, providing the external forces on the reduced grid of virtual points. Secondly, in order to transform the force into pressure, all the components of the reduced force vector are multiplied by

the scalar λ to convert them into pressure. Finally, the projection matrix is used to retrieve the distribution of pressure all over the surface of the layer.

An example of the reconstructed pressure wavefield is illustrated in Fig. 27. The wave coming from the top of the layer firstly creates a localized pressure field in the middle top part of it and, secondly, it travels along the sides of the layer. This behaviour has been recognized in all the performed tests. The piezoelectric sensors are subsequently excited from the top to the bottom of the layer. Due to reflection of the wavefield mentioned earlier in this section, a concentration of pressure is captured at the lower end of the panel until the measurement starts being affected by the mechanical behaviour of the sensing plate, as can be recognized also in the tail of the voltage time series showed in Fig. 26b.

5.3. *Pressure measurements validation and sensitivity study*

Validation of pressure measurements has been performed comparing the performance of the XPM10 pressure sensors with the retrofit layer. The locations of the three pressure sensors used as reference measurements are depicted in Fig. 27 by the red closed circles.

Fig. 28 shows the comparison of pressure signals measured by the two systems deployed.

Pressure signals at XPM1 position (Fig. 28a) show an overestimation of the pressure field measured by the retrofit layer. The bias in signal amplitude is believed to be the effect of the applied boundary condition in the performed experiment, i.e. clamps at the borders of the layer. The compressional force applied by the clamps at the borders of the layer might act as pre-load with a consequential pre-charge of the piezoelectric sensors located at the borders of the layer. As regards the phase of the signals, an overall agreement between the pressure sensor and the extracted pressure signals at XPM1 position has been reported. Nonetheless, it appears that the retrofit layer is less sensitive to instantaneous local variations of the pressure field. This effect is shown in Fig. 28a, between 200 and 300 ms.

Fig. 28b shows a slightly better agreement between the phases of the pressure signals. However, it appears that the retrofit layer detects the pressure field oscillations in advance with respect to the pressure sensor (e.g. between 200 and 300 ms). This effect might be due to the influence of the deformation of the host material (anticipating the local pressure measured by the pressure sensor) on the voltage measured by the piezoelectric sensors. As regards the amplitude of the pressure signals at XPM2 position, an overestimation can be noted in the pressure field measured by the retrofit layer. Also in this case, the deformation of the host material might have influenced the pressure field reconstruction performed by the retrofit layer. Note that XPM2 is located in the centre part of the layer. Considering the relatively higher difference in amplitude (e.g. around 200 ms, Fig. 28b) compared to the other locations, bending of the layer might have compromised the accuracy of the measurements even though the deployed support plate has been considered sufficiently stiff to limit the bending of the layer.

The pressure measurements at XPM3 position (Fig. 28c) show the best agreement in terms of amplitude of the two signals even if a slight misalignment between the two pressure signals is still evident. Also, it can be noted (around 350 ms) how the pressure signal extracted by the pressure field reconstruction with retrofit layer lacks in sensitivity to local fluctuations of the pressure field whilst detected by the pressure sensor.

A qualitative sensitivity study has been performed to evaluate the influence of disturbances that can be present in reality.

In order to characterize the experimental results with sufficient statistical representation, a group of 9 sensors is considered (n. 8–10; 13–15; 18–20) and the experiments have been repeated 25 times. Neglecting the non-working sensors (n. 18–19), the examined group is composed of seven piezoelectric transducers (Fig. 29).

For every test case, the 25 runs have been considered and for each run (in different conditions), the relevant negative peak of every sensors time series has been collected (Fig. 30). The average of the negative peaks of the group of sensors has been calculated and used as the index. The results for the considered 6 clusters of points are shown in Fig. 31.

For each cluster of points, the average of the plotted indices has been calculated. The average has been evaluated in terms of absolute value and plotted with the 95% confidence interval.

Fig. 32 reports the results of the sensitivity study. The reference Base case presents an absolute value of the average level of the response equal to 1.393 V with the lowest standard deviation, i.e. 0.085 V, providing the basis for comparison with the modified

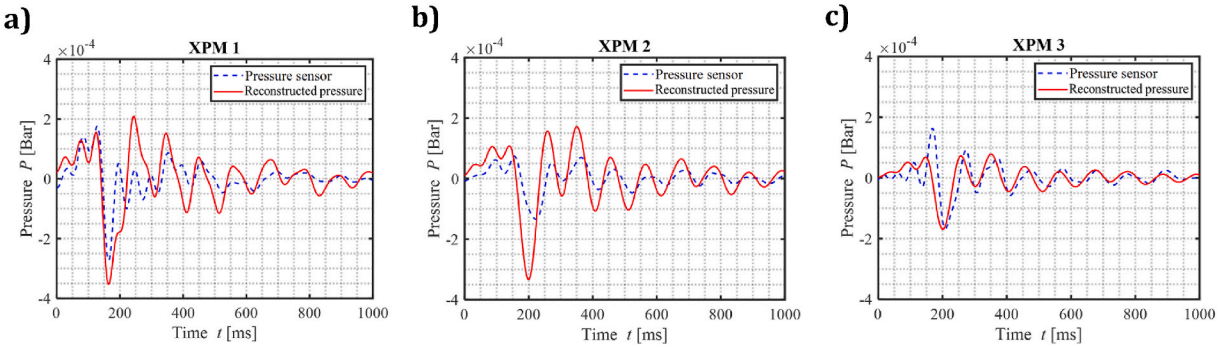

Fig. 28. Comparison of pressure signals measured by XPM10 and retrofit layer.

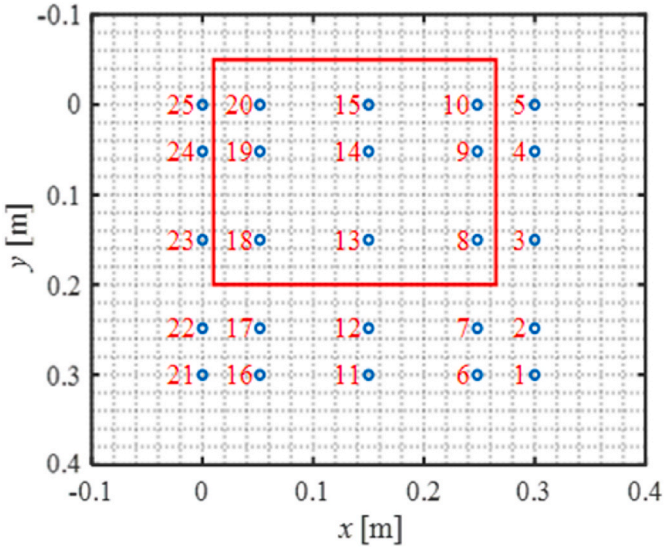

Fig. 29. Selected group of sensors.

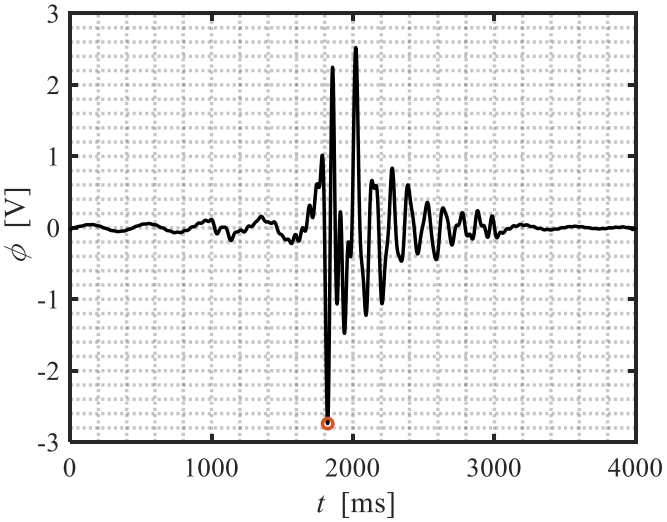

Fig. 30. Sample of relevant voltage peak.

condition tests.

Regarding the interference on the sensing surface, one ply of fabric does not affect the measurements in a relevant way. For this case, 1.385 V average level of the response has been reached with a standard deviation of 0.17 V. Considering two or three plies of fabric, the mean output level decreases causing losses of 10.10% and 25.57% from the original response respectively. Concerning the modification on the back of the layer, the two tested conditions introduce relevant bias in the measurements. The mean response level reaches 1.735 V for the three bands support plate test with 0.14 V standard deviation. At this point, it must be noted that all the above mentioned test cases are characterized by a relatively low dispersion of values showing an average standard deviation of 0.143 V. This changes to some extent when the last test case is considered. For this condition, the response level jumps to 2.85 V showing a higher standard deviation, i.e. 0.217 V. These two values are in line with the expectation that the absence of the support plate involves bending of the layer, contributing to the higher voltage output from the piezoelectric sensor. Furthermore, the lack of proper boundary conditions on the back of the layer has repercussions on the dispersion of the results because of the less controllable mechanical behaviour of the layer. Finally, a decreasing trend of the response is evident when considering a larger disturbance on the sensing surface. In summary, in case of bending of the layer, the voltage response is higher as well as the uncertainty of the measurements. The layer exhibits desirably-low sensitivity to disturbances on the sensing surface (e.g. marine growth). While it shows relatively high sensitivity to bending caused by imperfections in the mounting surface, therefore it needs to be placed very carefully on-board.

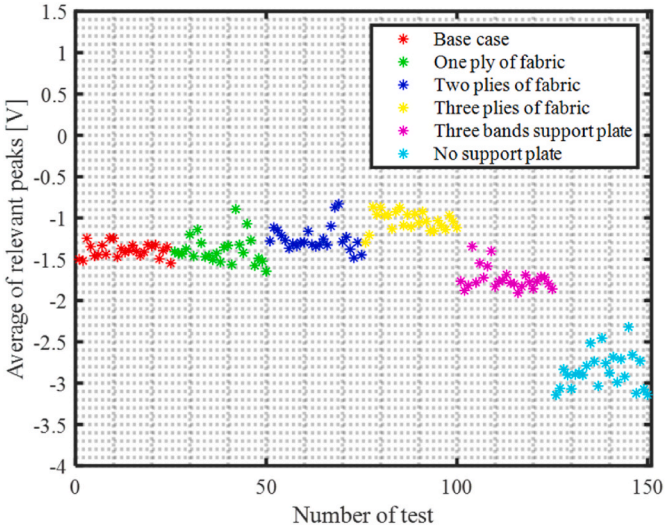

Fig. 31. Clusters of calculated indices.

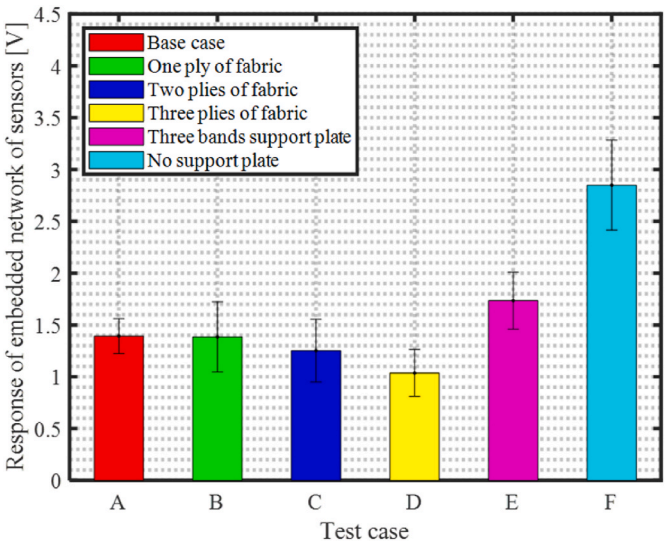

Fig. 32. Sensitivity study results.

6. Conclusions

Development of a retrofit layer with an embedded array of piezoelectric sensors for evaluation of the transient pressure field distribution was reported in this paper. A finite element-based inverse procedure to reconstruct the pressure field from the measured voltages has been formulated. Feasibility of the concept and sensitivity of the layer were assessed through experiments.

For the experimental validation, a 400 × 400 × 5 mm epoxy layer was fabricated embedding 25 piezoelectric sensors on a square grid in accordance with Gauss-Lobatto-Legendre points. Results from 2D FE simulations indicate that placing the embedded sensors 0.5 mm below the sensing surface of the layer increases its overall sensitivity if compared to other locations within the thickness of the layer.

To evaluate the capabilities of the layer, experiments were performed involving measurement and reconstruction of the pressure field generated by a travelling wave in a water tank. Starting from the measured voltages, the reconstruction of the pressure field was obtained using two mathematical operators (i.e. influence coefficients matrix and projection matrix). Additionally, a scalar conversion has been used to transform the external force into pressure.

A qualitative sensitivity study has been performed simulating the non-perfect conditions of the setup and evaluating the influence of disturbances that can be present in reality, such as debris on the layer and mounting surface imperfections.

Overall, the performed experiments served as proof of concept for the retrofit layer with embedded network of piezoelectric

sensors. The proposed concept demonstrated the capability to measure and reconstruct the transient pressure distribution despite the lack of sensitivity to very local pressure fluctuations when compared to the commercially available pressure sensors. In addition, the layer has shown relatively limited sensitivity to disturbances on the sensing surface while suffering from significant bias in the measurements when applied on non-flat surfaces.

Declaration of competing interest

The authors declare that they have no known competing financial interests or personal relationships that could have appeared to influence the work reported in this paper.

Data availability

Data will be made available on request.

Acknowledgements

This research was supported by Maritime Research Institute Netherlands (MARIN), Delft University of Technology (TU Delft) and University of Genova (UniGe).

References

[1] Yettou EM, Desrochers A, Champoux Y. Experimental study on the water impact of a symmetrical wedge. Fluid Dynam Res 2006;38(1):47–66. https://doi.org/10.1016/j.fluiddyn.2005.09.003.
[2] Lafeber FH, Van Wijngaarden E, Bosschers J. Computation of hull-pressure fluctuations due to non-cavitating propellers. 2009. Smp 2009, no. June.
[3] Ge M, Svennberg U, Bensow RE. Investigation on RANS prediction of propeller induced pressure pulses and sheet-tip cavitation interactions in behind hull condition. Ocean Eng 2020;209:107503. https://doi.org/10.1016/j.oceaneng.2020.107503. May.
[4] Garme K, Rosen A, Kuttenkeuler J. Detail investigation of planing pressure," HYDRALAB III Jt. User Meet. 2010. p. 1–4. February.
[5] Santoro N, Begovic E, Bertorello C, Bove A, De Rosa S, Franco F. Experimental study of the hydrodynamic loads on high speed planing craft. Procedia Eng 2014;88:186–93. https://doi.org/10.1016/j.proeng.2014.11.143.
[6] Swidan A, et al. Wetdeck slamming loads on a developed catamaran hullform–experimental investigation. Ships Offshore Struct 2017;12(5):653–61. https://doi.org/10.1080/17445302.2016.1194555.
[7] Shabani B, Lavroff J, Davis MR, Holloway DS, Thomas GA. Slam loads and pressures acting on high-speed wave-piercing catamarans in regular waves. Mar Struct 2019;66:136–53. https://doi.org/10.1016/j.marstruc.2019.03.007. May 2018.
[8] Lee I, Sung HJ. Development of an array of pressure sensors with PVDF film. Exp Fluid 1999;26(1–2):27–35. https://doi.org/10.1007/s003480050262.
[9] Foeth EJ, Bosschers J. Localization and source-strength estimation of propeller cavitation noise using hull-mounted pressure transducers. In: Proc. 31st Symp. Nav. Hydrodyn; 2016. p. 11–6. Monterey, CA, USA, no. September 2016.
[10] Van Wijngaarden E, Brouwer J, Zijlstra M. A spatial extrapolation technique for sparse measurements of propeller-induced hull-pressures using an inverse acoustic boundary element method. In: 6th Int. Symp. Cavitation CAV2006; September 2006. p. 1–9.
[11] Thomas G, et al. Slam events of high-speed catamarans in irregular waves. J Mar Sci Technol 2011;16(1):8–21. https://doi.org/10.1007/s00773-010-0105-y.
[12] Swidan A, et al. Experimental drop test investigation into wetdeck slamming loads on a generic catamaran hullform. Ocean Eng 2016;117:143–53. https://doi.org/10.1016/j.oceaneng.2016.03.059.
[13] Nikfarjam M, Yaakob OB, Seif MS, Koto J. Investigation of wedge water-entry under symmetric impact loads by experimental tests. Lat Am J Solid Struct 2017;14(5):861–73. https://doi.org/10.1590/1679-78253315.
[14] Bredmose H, Brocchini M, Peregrine DH, Thais L. Experimental investigation and numerical modelling of steep forced water waves. J Fluid Mech 2003;490(490):217–49. https://doi.org/10.1017/S0022112003005238.
[15] Akyildiz H, Erdem Ünal N. Sloshing in a three-dimensional rectangular tank: numerical simulation and experimental validation. Ocean Eng 2006;33(16):2135–49. https://doi.org/10.1016/j.oceaneng.2005.11.001.
[16] Brizzolara S, et al. Comparison of experimental and numerical sloshing loads in partially filled tanks. Ships Offshore Struct 2011;6(1–2):15–43. https://doi.org/10.1080/17445302.2010.522372.
[17] Pistani F, Thiagarajan K. Experimental measurements and data analysis of the impact pressures in a sloshing experiment. Ocean Eng 2012;52:60–74. https://doi.org/10.1016/j.oceaneng.2012.06.002.
[18] Kim SY, Kim KH, Kim Y. Comparative study on pressure sensors for sloshing experiment. Ocean Eng 2015;94:199–212. https://doi.org/10.1016/j.oceaneng.2014.11.014.
[19] Xue MA, Zheng J, Lin P, Yuan X. Experimental study on vertical baffles of different configurations in suppressing sloshing pressure. Ocean Eng 2017;136:178–89. https://doi.org/10.1016/j.oceaneng.2017.03.031. December 2015.
[20] Schreier S, Poelma C. A new generation of sloshing pressure sensors. 2018.
[21] Liu Y, Dai J, Zhang C. Real-time construction of sloshing-induced hydrodynamic field based on an intelligent image processing technique integrated with artificial damping model. Ocean Eng 2021;219:108382. https://doi.org/10.1016/j.oceaneng.2020.108382. October 2020.
[22] Patra JC. An artificial neural network-based smart capacitive pressure sensor. Meas. J. Int. Meas. Confed. 1997;22(3–4):113–21. https://doi.org/10.1016/S0263-2241(97)00074-2.
[23] Van den Bos A. Modeling of an intelligent pressure sensor using functional link artificial neural networks. ISA Trans 2000;39(1):15–27. https://doi.org/10.1016/S0019-0578(99)00035-X.
[24] Sinha S, Mandal N. Design of a smart pressure transmitter and its temperature compensation using artificial neural network. J. Control. Autom. Electr. Syst. 2019;30(1):95–103. https://doi.org/10.1007/s40313-018-00430-1.
[25] Fukushima H, Wakahara M, Kanai T. Hull surface pressure measurement of the affix-type multipoint pressure sensor using fiber bragg gratings. Lect. Notes Civ. Eng. 2021;63:368–83. https://doi.org/10.1007/978-981-15-4624-2_22. LNCE.
[26] Stagonas D, Marzeddu A, Cobos FXGI, Conejo ASA, Muller G. Measuring wave impact induced pressures with a pressure mapping system. Coast Eng 2016;112:44–56. https://doi.org/10.1016/j.coastaleng.2016.03.003.
[27] Marzeddu A, Stagonas D, Gironella X, Sánchez-Arcilla A. Experimental set-up and calibration errors for mapping wave-breaking pressures on marine structures. Ocean Eng 2018;151:115–26. https://doi.org/10.1016/j.oceaneng.2018.01.012. November 2017.
[28] Grigoropoulos GJ, Damala DP. Measurement of bottom pressures on planing craft. Comput Eng 2001;30:829–37. https://doi.org/10.2495/CMEM010811.
[29] Seok W, Park SY, Rhee SH. An experimental study on the stern bottom pressure distribution of a high-speed planing vessel with and without interceptors. Int J Nav Archit Ocean Eng 2020;12:691–8. https://doi.org/10.1016/j.ijnaoe.2020.08.003.

[30] Rosén A. Impact pressure distribution reconstruction from discrete point measurements. Int Shipbuild Prog 2005;52(1):91–107.
[31] Allen RG, Jones RR, Taylor DW. A Simplified Method for Determining Structural Design-Limit Pressures on High Performance Marine Vehicles 1978. https://doi.org/10.2514/6.1978-754.
[32] Hu N, Fukunaga H, Matsumoto S, Yan B, Peng XH. An efficient approach for identifying impact force using embedded piezoelectric sensors. Int J Impact Eng 2007;34(7):1258–71. https://doi.org/10.1016/j.ijimpeng.2006.05.004.
[33] Dessi D. Load field reconstruction with a combined POD and integral spline approximation technique. Mech Syst Signal Process 2014;46(2):442–67. https://doi.org/10.1016/j.ymssp.2014.01.005.
[34] Li Q, Lu Q. Force localization and reconstruction using a two-step iterative approach. JVC/Journal Vib. Control 2018;24(17):3830–41. https://doi.org/10.1177/1077546317713366.
[35] Dusek JE. Leading edge vortex detection using bio-inspired on-body pressure sensing. 2009.
[36] Fernandez VI, et al. Pressure sensor arrays to optimize the high speed performance of ocean vehicles. 11th Int. Conf. Fast Sea Transp. FAST 2011 - Proc 2011:363–70. August 2015.
[37] Maertens A. Touch at a distance: underwater object identification using pressure sensors. Ecole Polytech.; 2011. PhD Thesis.
[38] Dusek J, et al. Development and testing of bio-inspired microelectromechanical pressure sensor arrays for increased situational awareness for marine vehicles. Smart Mater Struct 2013;22(1). https://doi.org/10.1088/0964-1726/22/1/014002.
[39] Dusek JE, Triantafyllou MS, Lang JH. Piezoresistive foam sensor arrays for marine applications. Sensors Actuators, A Phys. 2016;248:173–83. https://doi.org/10.1016/j.sna.2016.07.025.
[40] Nakajima M, Wakahara M, Fukasawa T, Numata S. Development of a film-type pressure sensor using optical fiber with multiple fiber bragg gratings. 26th AIAA Aerodyn. Meas. Technol. Gr. Test. Conf., no. June 2008:1. https://doi.org/10.2514/6.2008-3949.
[41] Komoriyama Y, et al. Hull structural strength evaluation based on fiber bragg gratings pressure sensors to measure spatial pressure distribution on ship's hull in waves. Proc. Int. Conf. Offshore Mech. Arct. Eng. - OMAE 2020;2A:7372. https://doi.org/10.1115/omae2020-18434.
[42] Yoshimoto S, Kuroda Y, Oshiro O. Tomographic approach for universal tactile imaging with electromechanically coupled conductors. IEEE Trans Ind Electron 2020;67(1):627–36. https://doi.org/10.1109/TIE.2018.2879296.
[43] Van Oudheusden BW. PIV-based pressure measurement. Meas Sci Technol 2013;24(3). https://doi.org/10.1088/0957-0233/24/3/032001.
[44] Porfiri M, Shams A. Pressure reconstruction during water impact through particle image velocimetry: methodology overview and applications to lightweight structures. Dyn. Response Fail. Compos. Mater. Struct. 2017:395–416. https://doi.org/10.1016/B978-0-08-100887-4.00013-5.
[45] Jacobi G, Thill CH, van't Veer R, Huijsmans RHM. Analysis of the influence of an interceptor on the transom flow of a fast ship by pressure reconstruction from stereoscopic scanning PIV. Ocean Eng 2019;181:281–92. https://doi.org/10.1016/j.oceaneng.2019.02.062. February.
[46] Reddy JN. On laminated composite plates with integrated sensors and actuators. Eng Struct 1999;21:568–93. https://doi.org/10.1016/j.finel.2011.08.017.
[47] ANSI. IEEE standard on piezoelectricity. 1987 [Online]. Available:.
[48] Lin B, Giurgiutiu V. Modeling and testing of PZT and PVDF piezoelectric wafer active sensors. Smart Mater Struct 2006;15(4):1085–93. https://doi.org/10.1088/0964-1726/15/4/022.
[49] Gopalakrishnan S, Ruzzene M, Hanagud S. Computational techniques for structural health monitoring. 2011.
[50] Shin S, Zamorano B, Elvin N. Comparison of the electromechanical properties of embedded and surface-mounted piezoelectric transducers. J Intell Mater Syst Struct 2016;27(20):2837–50. https://doi.org/10.1177/1045389X16642299.
[51] Lam KY, Peng XQ, Liu GR, Reddy JN. A finite-element model for piezoelectric composite laminates. Smart Mater Struct 1997;6(5):583–91. https://doi.org/10.1088/0964-1726/6/5/009.
[52] Fernandes A, Pouget J. Analytical and numerical approaches to piezoelectric bimorph. Int J Solid Struct 2003;40(17):4331–52. https://doi.org/10.1016/S0020-7683(03)00222-1.
[53] Huijer AJ. Load and damage measurements on fibre-reinforced composites with embedded piezoelectric sensors: a feasibility study. 2019.
[54] Qi H, Fang D, Yao Z. FEM analysis of electro-mechanical coupling effect of piezoelectric materials. Comput Mater Sci 1997;8(4):283–90. https://doi.org/10.1016/s0927-0256(97)00041-4.
[55] Wang SY. A finite element model for the static and dynamic analysis of a piezoelectric bimorph. Int J Solid Struct 2004;41(15):4075–96. https://doi.org/10.1016/j.ijsolstr.2004.02.058.
[56] Xu B, Luan L, Chen H, Ge H. Numerical study on interface debonding detection mechanisms with 2D spectral element method for concrete-filled steel tube using embedded PZT sensor. Smart Mater Struct 2018;27(12). https://doi.org/10.1088/1361-665X/aae23b.
[57] Lin M, Chang FK. The manufacture of composite structures with a built-in network of piezoceramics. Compos Sci Technol 2002;62(7–8):919–39. https://doi.org/10.1016/S0266-3538(02)00007-6.
[58] Chilles JS, Croxford A, Bond IP. Design of an embedded sensor, for improved structural performance. Smart Mater Struct 2015;24(11). https://doi.org/10.1088/0964-1726/24/11/115014.
[59] Andreades C, Mahmoodi P, Ciampa F. Characterisation of smart CFRP composites with embedded PZT transducers for nonlinear ultrasonic applications. Compos Struct 2018;206:456–66. https://doi.org/10.1016/j.compstruct.2018.08.083. March.
[60] Lampani L, Sarasini F, Tirillò J, Gaudenzi P. Analysis of damage in composite laminates with embedded piezoelectric patches subjected to bending action. Compos Struct 2018;202:935–42. https://doi.org/10.1016/j.compstruct.2018.04.073. April.
[61] Scheyer AG, Anton SR. Impedance-based structural health monitoring of additive manufactured structures with embedded piezoelectric wafers. Sensors Smart Struct. Technol. Civil, Mech. Aerosp. Syst. 2017;10168:1016827. https://doi.org/10.1117/12.2260400. May.
[62] Patera AT. A spectral element method for fluid dynamics: laminar flow in a channel expansion. J Comput Phys 1984;54(3):468–88. https://doi.org/10.1016/0021-9991(84)90128-1.
[63] Komatitsch D, Vilotte JP. The spectral element method: an efficient tool to simulate the seismic response of 2D and 3D geological structures. Bull Seismol Soc Am 1998;88(2):368–92.
[64] Komatitsch D, Tromp J. Introduction to the spectral element method for three-dimensional seismic wave propagation. Geophys J Int 1999;139(3):806–22. https://doi.org/10.1046/j.1365-246X.1999.00967.x.
[65] Kudela P, Ostachowicz W. 3D time-domain spectral elements for stress waves modelling. J. Phys. Conf. Ser. 2009;181(1). https://doi.org/10.1088/1742-6596/181/1/012091.
[66] Lonkar K, Chang FK. Modeling of piezo-induced ultrasonic wave propagation in composite structures using layered solid spectral element. Struct Health Monit 2014;13(1):50–67. https://doi.org/10.1177/1475921713500514.
[67] Rupitsch SJ. Piezoelectric sensors and actuators. 2018.
[68] Kudela P. Parallel implementation of spectral element method for Lamb wave propagation modeling. Int J Numer Methods Eng 2015;(September):1413–29. https://doi.org/10.1002/nme.5119.
[69] PI. Piezoelectric ceramic products. 2020.
[70] PI. Material Data 2020. https://doi.org/10.1007/978-3-540-46585-0_14.
[71] USB-6211. Specifications. 2022.
[72] Meggit. Data for modelling. 2020.